










# Observational constraints on the stellar recycled gas in active galactic nuclei feeding

Rogério Riffel <sup>1,2\*</sup>, Luis G. Dahmer-Hahn,<sup>3</sup> Alexandre Vazdekis <sup>2,4</sup>, Richard Davies <sup>5</sup>,  
David Rosario <sup>6</sup>, Cristina Ramos Almeida <sup>2,4</sup>, Anelise Audibert,<sup>2,4</sup> Ignacio Martín-Navarro,<sup>2,4</sup>  
Lucimara Pires Martins,<sup>7</sup> Alberto Rodríguez-Ardila <sup>8,9,10</sup>, Rogemar A. Riffel <sup>11</sup>,  
Thaisa Storchi-Bergmann,<sup>1</sup> Michele Bertoldo-Coelho <sup>1</sup>, Marina Trevisan,<sup>1</sup> Erin Hicks,<sup>12</sup> Allan  
Schnorr-Müller <sup>1</sup>, Lais Nery Marinho<sup>1</sup> and Sylvain Veilleux<sup>13</sup>

*Affiliations are listed at the end of the paper*

Accepted 2024 May 1. Received 2024 April 30; in original form 2024 February 9

## ABSTRACT

Near-infrared long-slit spectroscopy has been used to study the stellar population (SP) of the low luminosity active galactic nuclei (AGNs) and matched analogues (LLAMA) sample. To perform the SP fits we have employed the X-shooter simple stellar population models together with the STARLIGHT code. Our main conclusions are: The star formation history of the AGNs is very complex, presenting many episodes of star formation during their lifetimes. In general, AGN hosts have higher fractions of intermediate-age SP (light-weighted mean ages,  $\langle t \rangle_L \lesssim 4.5$  Gyr) when compared with their analogues ( $\langle t \rangle_L \lesssim 8.0$  Gyr). AGNs are more affected by reddening and require significant fractions of featureless continuum and hot dust components. The ratio between the AGN radiated energy and the gravitational potential energy of the molecular gas ( $E_{\text{Rad}}/E_{\text{PG}}$ ) for the AGN is compared with the  $\langle t \rangle_L$  and a possible anticorrelation is observed. This suggests that the AGN is affecting the star formation in these galaxies, in the sense that more energetic AGN [ $\log(E_{\text{Rad}}/E_{\text{PG}}) \gtrsim 3$ ] tend to host nuclear younger SP ( $\langle t \rangle_L \lesssim 4$  Gyr). We found that the recent ( $t < 2$  Gyr) returned (recycled) stellar mass is higher in AGN than in the controls. We also provide evidence that the mass-loss of stars would be enough to feed the AGN, thus providing observational constraints for models that predict that AGN feeding is partially due to the recycled gas from dying stars.

**Key words:** galaxies: active – galaxies: evolution – galaxies: ISM – galaxies: star formation – galaxies: stellar content.

## 1 INTRODUCTION

From the seminal investigations that spotted the correlation between the mass of supermassive black holes (SMBHs) with the velocity dispersion of their host galaxy bulges, it has become accepted that there should be a connection between the active galactic nuclei (AGNs) accretion and star formation (SF) processes (e.g. Magorrian et al. 1998; Ferrarese & Merritt 2000; Gebhardt et al. 2000). Equally well-established is the coexistence of nuclear SF and AGN activity within the inner regions of galaxies, which strongly suggests a symbiotic relationship between the growth of SMBHs, through gas accretion, and the assembly of galaxies through SF (Heckman & Best 2014; Madau & Dickinson 2014, for a comprehensively review).

In the galaxy evolution framework, AGN is an important phase in the life cycle of a galaxy, during which its central SMBH accretes material from its vicinity, the circumnuclear environment (a few hundred pc). The amount of required material to fuel an AGN is

small<sup>1</sup> when compared with the amount of material available in the centers of spiral galaxies. The mechanism responsible for making this material lose angular momentum and ultimately feed the AGN is not a consensus (e.g. Silva-Lima et al. 2022), however, when falling into the deep potential well of an SMBH loses a huge amount of energy. Part of this energy is released in the form of radiation, winds, and relativistic jets.

Theoretical investigations and numerical simulations examining gas inflows in the vicinity of galactic nuclei have shown that they can give rise to episodes of SF, particularly in the nuclear region (e.g. Di Matteo, Springel & Hernquist 2005; Hopkins & Hernquist 2010; Zubovas et al. 2013; Heckman & Best 2014; Zubovas & Bourne 2017; Mercedes-Feliz et al. 2023; Weinberger et al. 2023). In this context, one of the most frequently invoked processes for regulating SF is AGN feedback (e.g. Terrazas et al. 2020, and references therein). According to some studies, the energy released by the AGN can heat the gas (or remove it) preventing SF (e.g. Granato et al. 2004; Fabian 2012; Zubovas et al. 2013; King & Pounds 2015; Zubovas &

<sup>1</sup>To sustain a Seyfert galaxy with a bolometric luminosity of  $10^{45}$  erg s<sup>-1</sup>, assuming a characteristic radiative efficiency of accretion of 10 per cent, only  $\sim 0.2 M_{\odot}$  yr<sup>-1</sup> are required (see Rosario et al. 2018).

\* E-mail: [riffel@ufrgs.br](mailto:riffel@ufrgs.br)

Bourne 2017; Trussler et al. 2020) or, as suggested in other studies, these outflows and jets, depending on the AGN luminosity, can compress the galactic interstellar medium, and therefore act as a catalyser, triggering or boosting the SF (e.g. Rees 1989; Hopkins 2012; Nayakshin & Zubovas 2012; Zubovas et al. 2013; Bieri et al. 2016; Zubovas & Bourne 2017) and even form stars inside the outflow [e.g. Ishibashi & Fabian 2012; Zubovas et al. 2013; El-Badry et al. 2016; Wang & Loeb 2018, for observational examples, see Maiolino et al. (2017); Gallagher et al. (2019)].

Mercedes-Feliz et al. (2023), using the cosmological hydrodynamical simulations from the feedback in realistic environment (FIRE), with a novel implementation of hyper-refined accretion-disc winds demonstrate that strong quasar winds, persisting for over 20 Myr, drive the formation of a central gas cavity and significantly reduce the surface density of SF across the galaxy’s disc. This shows that the suppression of SF occurs mainly by limiting the availability of gas for SF rather than by ejecting the pre-existing cold gas reservoir (preventive feedback dominates over ejective feedback). These authors also found that locally positive feedback is observed, in the sense that higher local SF efficiency is detected in compressed gas at the edge of the cavity produced by the winds from the central engine. Thus positive and negative feedback are taking place in different galaxy locations (e.g. Bessiere & Ramos Almeida 2022).

From observations, for instance, we have learned that nuclear SF is common in AGN (e.g. Terlevich, Diaz & Terlevich 1990; Storch-Bergmann et al. 2001; Cid Fernandes et al. 2004; Davies et al. 2007, 2009; Riffel et al. 2007, 2009, 2011b, 2016, 2021b, 2022, 2023b; Martins et al. 2010; Storch-Bergmann et al. 2012; Esquej et al. 2014; Ruschel-Dutra et al. 2017; Hennig et al. 2018; Mallmann et al. 2018; Burtscher et al. 2021; Dahmer-Hahn et al. 2022). However, comparing the AGN life-cycle ( $\sim 0.1$ – $10$  Myr; Novak, Ostriker & Ciotti 2011; Schawinski et al. 2015) with nuclear starbursts ages ( $\sim 1$ – $100$  Myr; Hickox et al. 2014) is very difficult, since the uncertainties associated with the latter may be larger than the AGN life-cycle. Studies have indicated that the proportion of young to intermediate-age stars in the vicinity of AGN is often correlated with the AGN’s luminosity. Typically, the most luminous AGN tend to exhibit higher fractions of these younger stellar populations (Cid Fernandes et al. 2004; Riffel et al. 2007, 2009; Ellison et al. 2016; Bessiere et al. 2017; Ruschel-Dutra et al. 2017; Zubovas & Bourne 2017; Mallmann et al. 2018; Ellison et al. 2021; Riffel et al. 2021b, 2023b). For instance, some studies have found that the age of the starburst is connected to the AGN’s luminosity (Davies et al. 2007; Riffel et al. 2022, 2023b), while no correlation between X-ray luminosity and the fraction of young stellar populations was identified in other analysis (Burtscher et al. 2021). It’s worth noting that the complexity of the results found in local AGN studies may partly stem from the luminosity acting as a ‘third parameter’, and the fact that studies on the optical bands may be strongly affected by reddening effects.

The stellar populations, consisting of stars with varying ages, metallicities, and formation histories, are the fundamental building blocks of galaxies. Analysing these stellar ensembles can offer critical insights into the evolutionary trajectories of galaxies, the dynamics of SF, and the role of feedback mechanisms in shaping the galaxies. Thus it is fundamental to investigate if there is an association between nuclear activity and SF, by studying the stellar population properties in the inner few tens of parsec of AGN over a wide range of AGN luminosities and comparing them with inactive sources with similar host galaxy properties. To disentangle the underlying continuum of AGN is a difficult task since at least three main components have to be fitted together, namely: the host galaxy stellar populations (characterized by their ages and metallicities), the

AGN accretion disc, and hot dust components (representing the torus emission, for details see Riffel et al. 2009). The wavelength region most sensitive to the AGN featureless components (accretion disc and hot dust emission) and the stellar population at the same time is the near-infrared ( $\text{NIR} \cong 0.8$ – $2.4 \mu\text{m}$ ) where the AGN featureless continuum (FC), the hot dust (HD), and the stellar population (SP) components can be fitted together and disentangled (Riffel et al. 2009, 2011b, 2022). Additionally, the NIR also offers the possibility to fit the stellar population content in the brighter type 1 sources, which in the optical will have their underlying stellar population out-shined by the accretion disc emission (e.g. Riffel et al. 2009).

One adequate sample to study the role played by the AGN and star-formation processes is the complete volume-limited sample of nearby AGN (selected by their 14–195 keV luminosity) with its control galaxies called *Low Luminosity AGN and Matched Analogues* sample (LLAMA, described in Davies et al. 2015). The stellar populations in the optical range of the type 2 LLAMA AGN and controls have been studied by Burtscher et al. (2021) who found that the young stellar populations are common inside the nuclear region of the AGN. However, they have shown that these young populations are not indicative of ongoing SF, but rather than to recent cessation in the star-formation providing evidence for models that see AGN activity as a consequence of nuclear SF. Building upon the previous study, here we study the nuclear stellar populations of the entire (type 1, type 2, and controls) LLAMA sample using NIR spectra, thus offering a more statistically complete analysis in a spectral region less sensitive to dust attenuation and sensitive to the three main components of the AGN spectral energy distribution. This paper is structured as follows: In Section 2 we present the sample observations and data reduction process. The fitting procedures are described in Section 3. Results are presented in Section 4. We discuss possible implications of the findings in Section 5 and conclusions at Section 6. Along this paper we have adopted in the calculations the galaxies distances listed by Davies et al. (2015) and the Kroupa (2001) initial mass function (IMF).

## 2 SAMPLE, OBSERVATIONS, AND DATA REDUCTION

### 2.1 The LLAMA sample of AGN and control galaxies

The selection of the sample, along with a well-matched control sample, holds the utmost importance in comprehending the impact of AGN activity on SF. Our study focuses on the LLAMA sample (Davies et al. 2015), which consists of 20 AGN meticulously chosen from the *Swift*/BAT all-sky ultra-hard X-ray (14–195 keV) survey in its 58-month edition (Ajello et al. 2012). The use of ultra-hard X-rays as a selection criterion presents a significant advantage, as it is mainly unaffected by obscuration, except for the most heavily obscured sources known as Compton-thick (e.g. LaMassa et al. 2010; Sales et al. 2011, 2014; Ricci et al. 2015). According to Martini et al. (2003), the less luminous the AGN are, the more diverse the fuelling mechanism becomes. To focus on ‘genuine’ AGN, which are more likely to be fuelled by a unified mechanism, we selected the most luminous sources ( $\log L_X/(\text{erg/s}) > 42.5$ ). Moreover, we further refine our selection to include only local AGN ( $z < 0.01$ ), corresponding to distances of approximately  $\leq 40$  Mpc or less, giving us access to a scale of up to a few hundred parsecs ( $\lesssim 200$  pc).

Additionally, the LLAMA sample incorporates a control group of 19 galaxies chosen to match the AGN sample in terms of distance, Hubble type, stellar mass (measured by *H* band luminosity), and axis ratio (inclination). This matched control sample plays a vital

**Table 1.** Main properties of our sample and observations.

(1) Source	(2) RA (h:m:s)	(3) DEC (d:m:s)	(4) K (mag)	(5) z	(6) D (Mpc)	(7) Morph.	(8) Instrument/ Telescope	(9) Slit Width (arcsec)	(10) Aperture (arcsec)	(11) P.A. (deg)
Sample										
NGC 1365	03:33:36.4	−36:08:26.3	6.373	0.00546	18	Sb	Tspec/Blanco <sup>1</sup>	1.1	2.0	0
MCG-05-14-012	05:43:32.9	−27:39:05.0	10.80	0.00992	41	S0 <sup>+</sup>	Tspec/SOAR <sup>2</sup>	1.1	2.0	80
NGC 2110	05:52:11.3	−07:27:22.4	8.140	0.00765	34	S0 <sup>−</sup>	SpeX/IRTF <sup>5</sup>	0.8	1.5	20
NGC 2992	09:45:42.0	−14:19:34.9	8.590	0.00771	36	Sa	SpeX/IRTF <sup>3</sup>	0.8	2.0	50
MCG-05-23-016	09:47:40.1	−30:56:55.9	9.349	0.00849	35	S0 <sup>+</sup>	Tspec/SOAR <sup>2</sup>	1.1	2.0	45
NGC 3081	09:59:29.5	−22:49:34.7	8.910	0.00798	34	S0/A	Tspec/Blanco <sup>4</sup>	1.1	2.0	90
NGC 3783	11:39:01.7	−37:44:19.0	8.649	0.00973	38	Sab	Tspec/SOAR <sup>2</sup>	1.1	2.0	90
NGC 4235	12:17:09.8	+ 07:11:29.6	8.396	0.00755	37	Sa	GNIRS/GEMINI <sup>6</sup>	0.3	1.8	113
NGC 4388	12:25:46.8	+ 12:39:43.4	8.004	0.00842	39	Sb	GNIRS/GEMINI <sup>6</sup>	0.3	1.8	64
NGC 4593	12:39:39.4	−05:20:39.0	7.985	0.00831	37	Sb	Tspec/SOAR <sup>2</sup>	1.1	2.0	40
NGC 5128	13:25:27.6	−43:01:08.8	3.942	0.00183	3.8	S0 <sup>0</sup>	Tspec/SOAR <sup>2</sup>	1.1	2.0	135
ESO 021-G004	13:32:40.6	−77:50:40.8	8.248	0.00984	39	S0/a	Tspec/SOAR <sup>2</sup>	1.1	2.0	100
MCG-06-30-015	13:35:53.7	−34:17:44.1	9.582	0.00775	27	E	Tspec/SOAR <sup>2</sup>	1.1	2.0	90
NGC 5506	14:13:14.9	−03:12:27.2	8.188	0.00608	27	Sa	Tspec/SOAR <sup>2</sup>	1.1	2.0	90
NGC 5728	14:42:23.9	−17:15:11.4	8.171	0.00932	39	Sa	SpeX/IRTF <sup>5</sup>	0.8	1.5	36
ESO 137-G034	16:35:14.1	−58:04:48.1	8.258	0.00914	35	S0/a	Tspec/SOAR <sup>2</sup>	1.1	2.0	0
NGC 6814	19:42:40.5	−10:19:25.1	7.657	0.00522	23	Sbc	SpeX/IRTF <sup>7</sup>	0.8	3.7	0
NGC 7172	22:02:01.8	−31:52:11.6	8.317	0.00868	37	Sab	Tspec/Blanco <sup>1</sup>	1.1	2.0	97
NGC 7213	22:09:16.2	−47:10:00.0	7.035	0.00584	25	Sa	Tspec/Blanco <sup>1</sup>	1.1	2.0	113
NGC 7582	23:18:23.6	−42:22:14.0	7.316	0.00525	22	Sab	Tspec/Blanco <sup>1</sup>	1.1	2.0	119
Control sample										
NGC 0718	01:53:13.3	+ 04:11:45.3	8.739	0.00578	23	Sa	Tspec/Blanco <sup>1</sup>	1.1	2.0	135
NGC 1079	02:43:44.3	−29:00:11.7	8.344	0.00484	19	S0/a	Tspec/SOAR <sup>2</sup>	1.1	2.0	90
NGC 1315	03:23:06.6	−21:22:30.7	9.734	0.00539	21	S0 <sup>+</sup>	Tspec/SOAR <sup>2</sup>	1.1	2.0	90
NGC 1947	05:26:47.6	−63:45:36.0	7.497	0.00367	19	S0 <sup>−</sup>	Tspec/SOAR <sup>2</sup>	1.1	2.0	90
ESO 208-G021	07:33:56.2	−50:26:35.0	7.878	0.00362	17	S0 <sup>−</sup>	Tspec/SOAR <sup>2</sup>	1.1	2.0	110
NGC 2775	09:10:20.1	+ 07:02:16.5	7.037	0.00450	21	Sab	Tspec/SOAR <sup>2</sup>	1.1	2.0	90
NGC 3175	10:14:42.1	−28:52:19.4	7.786	0.00363	14	Sa	Tspec/SOAR <sup>2</sup>	1.1	2.0	45
NGC 3351	10:43:57.7	+ 11:42:13.0	6.665	0.00260	11	Sb	Tspec/SOAR <sup>2</sup>	1.1	2.0	110
ESO 093-G003	10:59:26.0	−66:19:58.3	8.621	0.00611	22	S0/a	Tspec/SOAR <sup>2</sup>	1.1	2.0	135
NGC 3717	11:31:31.9	−30:18:27.8	7.518	0.00578	24	Sb	Tspec/SOAR <sup>2</sup>	1.1	2.0	90
NGC 3749	11:35:53.2	−37:59:50.3	8.705	0.00901	42	Sa	Tspec/SOAR <sup>2</sup>	1.1	2.0	120
NGC 4224	12:16:33.7	+ 07:27:43.6	8.609	0.00862	41	Sa	Tspec/SOAR <sup>2</sup>	1.1	2.0	60
NGC 4254	12:18:49.6	+ 14:24:59.3	6.929	0.00803	15	Sc	Tspec/SOAR <sup>2</sup>	1.1	2.0	90
NGC 4260	12:19:22.2	+ 06:05:55.6	8.538	0.00592	31	Sa	Tspec/SOAR <sup>2</sup>	1.1	2.0	50
NGC 5037	13:14:59.3	−16:35:25.1	8.599	0.00619	35	Sa	Tspec/SOAR <sup>2</sup>	1.1	2.0	45
NGC 5845	15:06:00.7	+ 01:38:01.7	9.112	0.00555	25	E	Tspec/SOAR <sup>2</sup>	1.1	2.0	135
NGC 5921	15:21:56.5	+ 05:04:13.9	8.096	0.00494	21	Sbc	Tspec/SOAR <sup>2</sup>	1.1	2.0	20
IC 4653	17:27:06.9	−60:52:44.1	10.08	0.00640	26	S0/a	Tspec/SOAR <sup>2</sup>	1.1	2.0	131
NGC 7727	23:39:53.8	−12:17:34.8	7.688	0.00599	26	Sa	Tspec/Blanco <sup>1</sup>	1.1	2.0	10

*Notes.* (1) Galaxy name; (2) Right Ascension; (3) Declination; (4) K band magnitude (Jarrett et al. 2003); (5) Redshift taken from NED (<https://ned.ipac.caltech.edu/>); (6) Distance from Davies et al. (2015); (7) Morphology, as compiled by Davies et al. (2015) and converted to De Vaucouleurs (1959) system; (8) Spectrograph and telescope used; (9) Slit width of the instrument; (10) Aperture integrated for final spectra; (11) Position angle of the slit, in degrees East of North.

<sup>1</sup> Obtained under project 2016B-0912; <sup>2</sup> Obtained under project SO2021B-004; <sup>3</sup> Obtained under project 2017A022; <sup>4</sup> Obtained under project 2016A-0621; <sup>5</sup> Data published by Riffel, Rodríguez-Ardila & Pastoriza (2006); <sup>6</sup> Data published by Mason et al. (2015); <sup>7</sup> Data published by Riffel et al. (2019).

role within the LLAMA framework, as it enables us to calibrate our results against a comparable set of galaxies that solely differ from the AGN sample in terms of their nuclear accretion rate. We consider this control sample selection integral to the overall integrity and robustness of the LLAMA project. The main properties of the sample are summarized in Table 1. For more details see Burtscher et al. (2021) and Davies et al. (2015).

## 2.2 Observations and data reduction

Out of our sample, five AGNs had literature spectra available (taken from Riffel et al. 2006; Mason et al. 2015; Riffel et al. 2019, see Table 1 for more details). A detailed discussion of their observations

and reductions can be found in their respective papers, but they followed the standard observation and reduction processes for the NIR (see discussion below for our sample).

The remaining 15 AGNs and 19 controls were observed as part of this work, employing either the SpeX spectrograph attached to the Infrared Telescope Facility (IRTF; Rayner et al. 2003), or employing the Triplespec 4 spectrograph, which was mounted on the Victor M. Blanco telescope until 2019 (where it was named ARCoIRIS), or mounted on the SOAR telescope since then (and where it is named TripleSpec 4.1). From now on, we refer to Triplespec 4 as Tspec, regardless of which telescope it was mounted on. During daytime calibrations, we took flat fields and hollow cathode lamps (CuHeAr), in order to correct for discrepancies in sensitivity between pixels and

to wavelength calibrate the target. Galaxies were observed using either ABBA pattern (i.e. nodding the object along the slit), or observed in an A-Sky-A pattern, to remove sky emission. Also, each galaxy observed was preceded or followed by an A0V star with similar airmass, which was then used to remove telluric absorptions, as well as to flux calibrate the spectra. Lastly, although we observed hollow arcs during daytime, the objects were  $\lambda$ -calibrated using sky emission lines, which are more reliable than arcs because they are taken at the same time as the target.

Both SpeX and Tspec standard data reduction is performed using the SPECTOOL IDL package (Vacca, Cushing & Rayner 2003; Cushing, Vacca & Rayner 2004). This pipeline follows the standard NIR data reduction process and consists of flat-field correction, sky subtraction, a combination of observations to improve the signal-to-noise (S/N) ratio, wavelength calibration, telluric absorptions correction, merging of the different orders, and flux calibration employing the same A0V correction.

After the data reduction, we corrected our spectra for galactic reddening using a Cardelli, Clayton & Mathis (1989, hereafter CCM) law, and then corrected for redshift (this was done also for the literature data) and homogenized the spectral resolution of them. An example of the final reduced spectra for four galaxies, namely: NGC 3081 (AGN), NGC 2992 (AGN), IC 4653 (control galaxy, hereafter CNT), and NGC 0718 (CNT) are shown in Fig. 1, together with the identification of the most prominent absorption- and emission-line features. The remaining sources are shown as supplementary material. Observing information and some general properties of the galaxies are shown in Table 1 with a full description of the sample made in Davies et al. (2015). The main AGN properties are shown in Table 2.

### 3 STELLAR POPULATION FITTING

The integrated spectra of galaxies are comprised of various components, including for example the underlying stellar, gas, and dust emission contributions (Bica & Alloin 1987; Schmidt et al. 1991; Riffel et al. 2009, 2011b, 2022; Walcher et al. 2011; Conroy 2013; Gomes & Papaderos 2017, and references therein). In the case of active galaxies, additional considerations must be given to components such as the AGN torus and accretion disc (Riffel et al. 2009, 2022; Burtscher et al. 2015). The process of stellar population fitting involves determining the percentage contribution of these components to the integrated spectrum.

It is important to note that due to the large number of parameters involved (such as age, metallicity, kinematics, reddening, and AGN components), numerous techniques have been employed over the years to separate the different components of a galaxy's spectrum (see Walcher et al. 2011; Conroy 2013, for a review). As a result, various fitting codes have been developed by different research groups, each with their own priorities in mind (e.g. Cid Fernandes et al. 2005; Ocvirk et al. 2006; Tojeiro et al. 2007; Koleva et al. 2009; Sánchez et al. 2016; Cappellari 2017; Gomes & Papaderos 2017; Wilkinson et al. 2017; Johnson et al. 2021). Naturally, comparisons among these different codes have been conducted, demonstrating that, in general, the codes yield consistent results when applied to the same data with the same input parameters (e.g. Koleva et al. 2008; Dias et al. 2010; Goddard et al. 2017; Gomes & Papaderos 2017; Cid Fernandes 2018; Ge et al. 2018; Woo et al. 2024).

For the purpose of conducting stellar population fitting, we use the software STARLIGHT (Cid Fernandes et al. 2004, 2005; Asari et al. 2007; Cid Fernandes 2018). We opted for this particular choice primarily to ensure consistency with previous studies conducted by our

team, enabling easier comparisons of the results. The STARLIGHT code fits the complete absorption and continuum features in the observed spectra by combining in different proportions the base-set elements. It excludes emission lines and spurious data, employing a blend of computational techniques derived from semi-empirical population synthesis and evolutionary synthesis models (Cid Fernandes et al. 2004, 2005).

In essence, the code fits an observed spectrum, represented as  $O_\lambda$ , using a combination of  $N_*$  simple stellar populations (SSPs) in varying proportions. The visual extinction ( $A_V$ ) is modelled by STARLIGHT as foreground dust lanes. In the fits we use the CCM (Cardelli et al. 1989) extinction law. The modelled spectrum,  $M_\lambda$ , is obtained through the following equation:

$$M_\lambda = M_{\lambda_0} \sum_{j=1}^{N_*} x_j b_{j,\lambda} r_\lambda \otimes G(v_*, \sigma_*), \quad (1)$$

where  $x_j$  is the population vector,  $b_{j,\lambda}$  is the  $j$ th base element (see below),  $r_\lambda$  is the reddening factor of the  $j$ th component normalized at  $\lambda_0$ , the reddening term is represented by  $r_\lambda = 10^{-0.4(A_\lambda - A_{\lambda_0})}$ ,  $M_{\lambda_0}$  is the synthetic flux at the normalization wavelength (we have used  $\lambda_{\text{norm}} = 12\,230 \text{ \AA}$  in the rest frame). The convolution operator is  $\otimes$  and  $G(v_*, \sigma_*)$  is the Gaussian distribution used to model the line-of-sight velocity distributions of the stars, which is centred at velocity  $v_*$  with dispersion  $\sigma_*$ . The final fit is carried out through a chi-square minimization, as follows:

$$\chi^2 = \sum_{\lambda} [(O_\lambda - M_\lambda) w_\lambda]^2, \quad (2)$$

where emission lines and spurious features are excluded from the fit by fixing  $w_\lambda = 0$  at the corresponding wavelengths.

For the base of elements, in this paper, we used as simple stellar population (SSP) the evolutionary population synthesis (EPS) models of Verro et al. (2022b). These models have been computed with the new X-shooter Spectral Library (XSL; Verro et al. 2022a). The base of elements comprises SSPs with four metallicities ( $Z = 0.25, 0.63, 1, \text{ and } 1.53 Z_\odot$ ) and 25 ages ( $t = 0.050, 0.063, 0.079, 0.1, 0.126, 0.158, 0.200, 0.251, 0.316, 0.398, 0.501, 0.631, 0.794, 1, 1.259, 1.585, 1.995, 2.512, 3.162, 3.981, 5.012, 6.310, 7.943, 10, \text{ and } 12.589 \text{ Gyr}$ ). They have been selected to have Kroupa (2001) IMF and the PARSEC/COLIBRI isochrones (Chen et al. 2015; Pastorelli et al. 2020), cover younger ages and are on the models safe-range (see fig. 19 of Verro et al. 2022b).

Additionally, to account for the accretion disc featureless continuum (FC) we have used a power law of the form  $F_\lambda \propto \lambda^{-\alpha}$  (e.g. Koski 1978; Cid Fernandes et al. 2005; Riffel et al. 2009). We employed three different values for  $\alpha$ , namely: 0.25, 0.5, and 0.75. To properly account for the hot dust emission component, eight Planck distributions (black-body, BB), with temperatures ranging from 700 K to 1400 K, in steps of 100 K, were included in the fits. The lower limit was chosen because lower temperatures are hard to detect in this spectral range (Riffel et al. 2009) and the upper limit is very close to the sublimation temperature of the dust grains (e.g. Barvainis 1987; Granato & Danese 1994). For more details on the effects of these components in the NIR spectra and on the definition of our base of elements see Riffel et al. (2009, 2022). The components used in the fits are shown in Fig. 2.

#### 3.1 Uncertainties on the fits

Statistical analysis plays a crucial role in interpreting spectral fitting findings, as evident from its widespread application (e.g. Panter



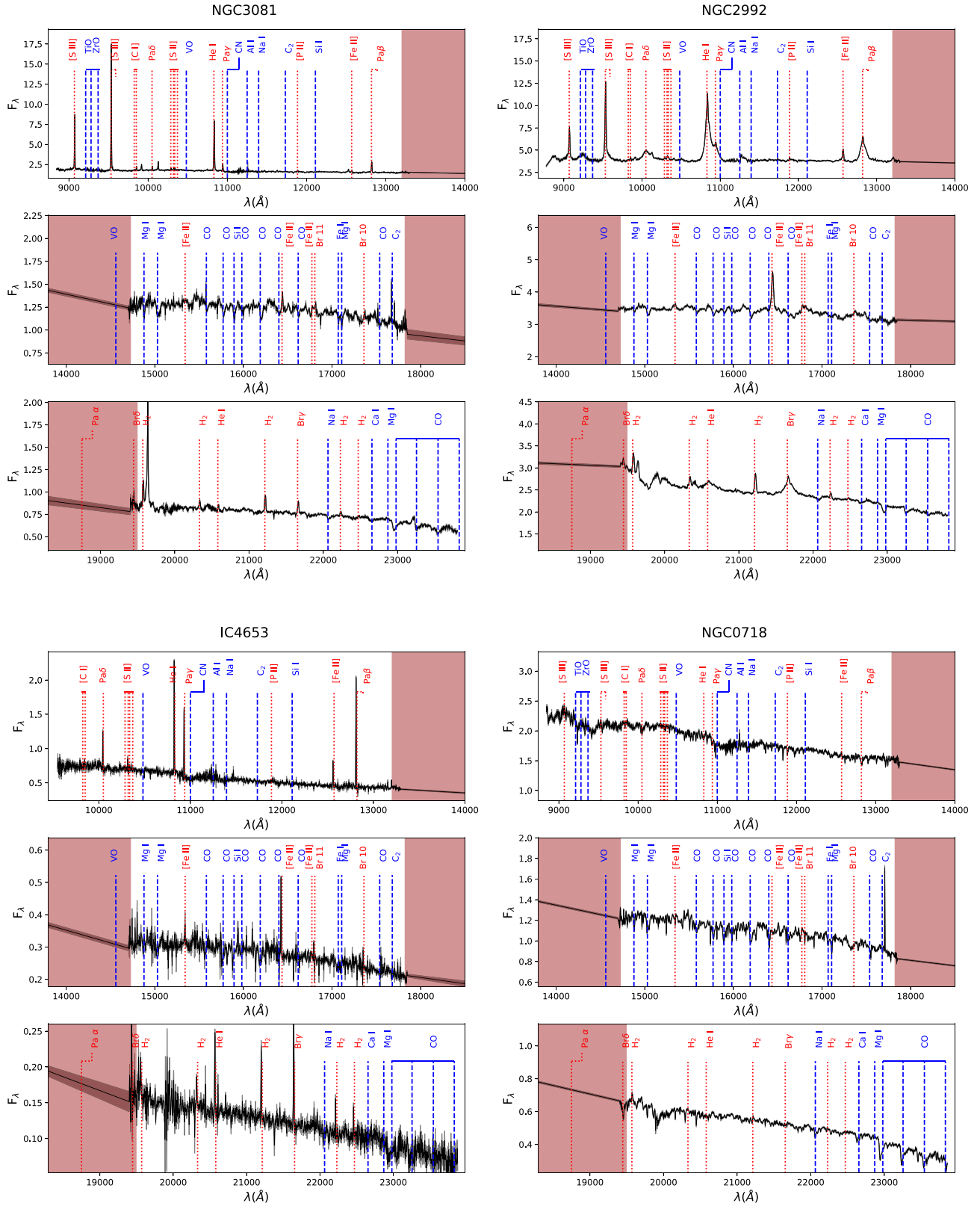


**Figure 1.** Final reduced and redshift-corrected spectra for NGC 3081 (AGN), NGC 2992 (AGN), IC 4653 (CNT), and NGC 0718 (CNT). For each galaxy we show – the redshift and reddening corrected spectra – from top to bottom the, *J*, *H*, and *K* bands, respectively. The flux is in units of  $10^{-15}$  erg  $\text{cm}^{-2}$   $\text{s}^{-1}$ . The shaded grey area represents the uncertainties and the brown area indicates the poor transmission regions between different bands. The remaining spectra are shown in on-line material.

**Table 2.** Main AGN properties.

Source (1)	Activity Type (2)	$L_X^{\text{obs}}$ erg s <sup>-1</sup> (3)	$L_X^{\text{int}}$ erg s <sup>-1</sup> (4)	$M_{\text{SMBH}}$ 10 <sup>6</sup> M <sub>⊙</sub> (5)	log $L_H$ L <sub>⊙</sub> (6)	log $N_H$ cm <sup>-2</sup> (7)	log( $L'_{\text{CO}}$ ) K km s <sup>-1</sup> pc <sup>2</sup> (8)	log $L_{[\text{O III}]}$ erg s <sup>-1</sup> (9)	log $L_{H_2}$ erg s <sup>-1</sup> (10)
ESO021-G004	Sy 2	42.56	42.70	52.1 ± 38.4 <sup>3</sup>	10.53	23.8	8.083	38.68 ± 0.46	–
ESO137-G034	Sy 2	42.71	42.76	21.5 ± 15.8 <sup>3</sup>	10.44	24.3	7.820	40.66 ± 0.45	38.81 ± 0.45
MCG-05-14-012	Sy 1.0	42.64	42.65	2.29 ± 0.68 <sup>1</sup>	9.60	≤21.9	–	39.21 ± 0.46	–
MCG-05-23-016	Sy 1.9	43.51	43.50	27.1 ± 8.74 <sup>1</sup>	9.94	22.2	7.445	39.62 ± 0.46	38.31 ± 0.45
MCG-06-30-015	Sy 1.2	42.92	42.91	7.38 ± 1.98 <sup>1</sup>	9.59	20.9	7.109	39.65 ± 0.47	37.62 ± 0.45
NGC1365	Sy 1.8	42.63	42.60	19.7 ± 5.77 <sup>1</sup>	10.58	22.2	8.782	–	38.12 ± 0.45
NGC2110	Sy 2	43.63	43.63	150 ± 110 <sup>3</sup>	10.44	23.0	7.603	40.15 ± 0.45	39.11 ± 0.46
NGC2992	Sy 1.8	42.55	42.52	22.8 ± 6.74 <sup>1</sup>	10.31	21.7	8.472	39.99 ± 0.45	39.26 ± 0.46
NGC3081	Sy 2	43.07	43.29	36.6 ± 26.9 <sup>3</sup>	10.15	23.9	7.749	40.57 ± 0.45	38.73 ± 0.45
NGC3783	Sy 1.2	43.58	43.58	11.2 ± 3.61 <sup>1</sup>	10.29	20.5	7.955	40.76 ± 0.45	38.02 ± 0.45
NGC4235	Sy 1.2	42.66	42.64	55.8 ± 15.9 <sup>1</sup>	10.43	21.3	7.754	39.39 ± 0.45	–
NGC4388	Sy 2	43.64	43.70	8.40 ± 0.2 <sup>2</sup>	10.65	23.5	8.151	–	39.00 ± 0.46
NGC4593	Sy 1.0/1.2	43.20	43.20	12.4 ± 3.91 <sup>1</sup>	10.59	≤19.2	8.146	39.70 ± 0.45	–
NGC5128	Sy 2	43.00	43.02	66.3 ± 48.9 <sup>3</sup>	10.22	23.1	–	–	37.12 ± 0.46
NGC5506	Sy 2	43.31	43.30	22.4 ± 17.2 <sup>3</sup>	10.09	22.4	7.874	–	38.74 ± 0.45
NGC5728	Sy 2	43.23	43.36	23.0 ± 2.3 <sup>2</sup>	10.56	24.2	8.531	40.50 ± 0.45	39.04 ± 0.46
NGC6814	Sy 1.5	42.76	42.75	11.6 ± 3.67 <sup>1</sup>	10.31	21.0	7.491	39.57 ± 0.45	37.73 ± 0.45
NGC7172	Sy 2	43.46	43.32	53.4 ± 39.3 <sup>3</sup>	10.43	22.9	8.658	38.60 ± 0.45	–
NGC7213	Sy 1	42.50	42.49	6.46 ± 2.01 <sup>1</sup>	10.62	≤20.4	7.959	39.26 ± 0.45	38.47 ± 0.45
NGC7582	Sy 2	42.68	43.29	30.5 ± 22.4 <sup>3</sup>	10.38	24.2	8.917	39.29 ± 0.45	38.38 ± 0.45

*Note.* (1) Source name; (2) Activity type, as compiled by Davies et al. (2015), with the exception of ESO021-G004, whose classification was taken from Burtscher et al. (2021); (3) Logarithm of the observed hard X-ray luminosity (14–195 keV) from Ricci et al. (2017); (4) Logarithm of the intrinsic hard X-ray luminosity (14–195 keV) from Ricci et al. (2017); (5) The Black Hole mass, published by Caglar et al. (2020), derived from: <sup>1</sup>broad H $\alpha$  emission, <sup>2</sup>megamaser or <sup>3</sup>stellar velocity dispersion; (6) Integrated  $H$ -band luminosity (given by the 2MASS total magnitude Skrutskie et al. 2006); (7) Neutral absorbing column, from Ricci et al. (2015), based on modeling 0.3–150 keV spectrum; (8) The CO luminosities, from Rosario et al. (2018); (9) Measured [O III] luminosity, and (10) Measured H<sub>2</sub> luminosity.

et al. 2007). The practice of averaging results serves to diminish uncertainties (Cid Fernandes et al. 2013). Incorporating statistical interpretation is also advantageous for generating uncertainty estimations, a feature not readily available in STARLIGHT standard output.

A viable approach to obtain such estimations involves perturbing the input spectra, considering realistic error prescriptions (Cid Fernandes et al. 2013). Here we followed Dametto et al. (2014) and simulated 100 spectra for each galaxy within our sample employing Monte Carlo approach. The simulated flux for each wavelength ( $\lambda_i$ ) is computed assuming a Gaussian distribution of the uncertainties, being the mean flux in each  $\lambda_i$  the measured flux ( $F_{\lambda_i}$ ) value, and the standard deviation is given by the errors derived in the data reduction (which include the propagation of uncertainties over all the data reduction steps).

During its likelihood-guided sampling process of the parameter space, STARLIGHT offers a single best-fitting set of parameters from the numerous trials during the fitting process. Nevertheless, it is important to note that these individual solutions may not always be mathematically unique. In light of this, we proceeded with stellar population fitting on all the simulated spectra, aiming to derive an average value for each galaxy, along with the associated standard deviation. This approach allows us to gain a more robust and comprehensive understanding of the results, considering the inherent uncertainties present in the analysis.

## 4 RESULTS

### 4.1 Fitting approach

The results of the stellar population fitting are the fractional contributions, in light and mass (in the case of the stellar ones), of

each one of the base components (the so-called population vector). They can be separated into stellar population components and AGN components. An example of the results of the fitting, the population vectors, binned population vectors (see below), as well as mean ages and metallicities are shown in Fig. 3, where we show the fits for four sources, namely NGC 3081, NGC 4235, IC 4653, and NGC 0718, two AGN hosts and two control sources, respectively. For each galaxy, we show on the *upper top panel* the observed spectrum (black) and the synthetic spectrum (red); in the *middle panel* the ‘pure’ emission-spectrum (difference between the observed and synthetic spectrum). On the *bottom panel*: from left to right, SFH summed over all metallicities in light ( $x$ ) and mass ( $\mu$ ) fractions; SFH considering different metallicities (they are labelled); binned population vectors (see below); AGN FC continuum and HD contributions are on the two last panels. The plots for the remaining spectra are shown in the supplementary material.

To consider the impact of noise on the data, which can obscure differences between similar spectral components, as well as the age-metallicity degeneracy (e.g. Worthey et al. 1994), besides the approach presented in Section 3.1 we also adopted the approach used by Cid Fernandes et al. (2005) and used the *binned* (or condensed) population vectors<sup>2</sup> as defined in Riffel et al. (2009, 2022):

$xy$ : sum of the percent contribution of SSPs with ages  $50 \leq t \leq 100$  Myr. This vector is representative of the younger (ionizing) population.<sup>3</sup>

<sup>2</sup>By binning the data, we obtain coarser but more reliable fractions for each bin, thereby accounting for uncertainties arising from noise effects and spectral similarities.

<sup>3</sup>Note however that it is limited by the younger age available in the XSL models.

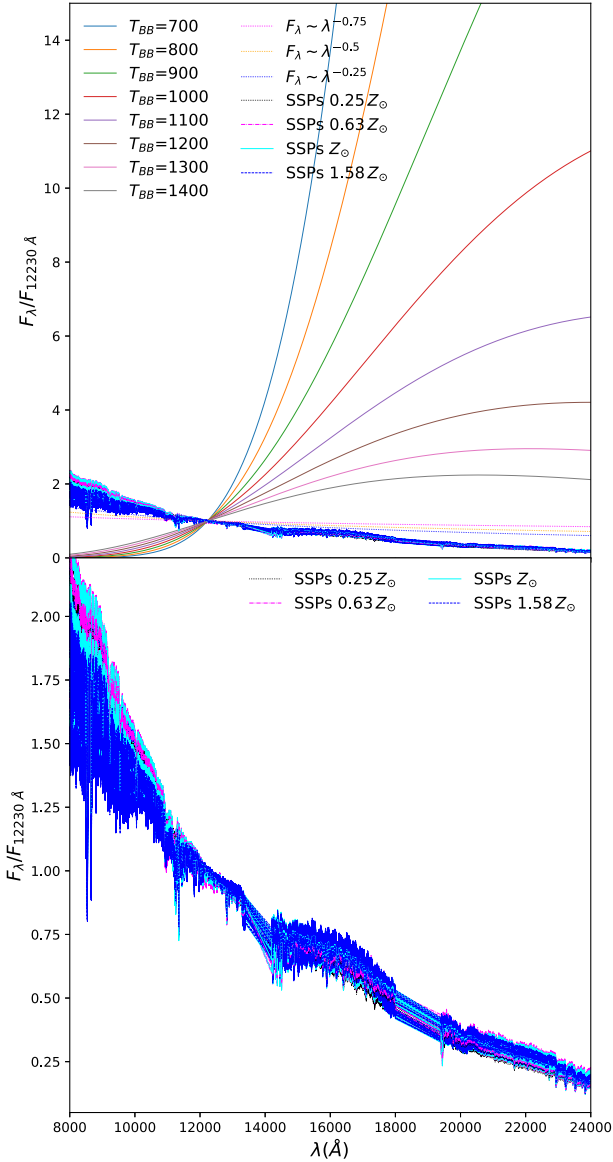


**Figure 2.** The base of elements comprises SSPs with four metallicities ( $Z = 0.25, 0.63, 1, \text{ and } 1.53 Z_{\odot}$ ) and 25 ages ( $t = 0.050, 0.063, 0.079, 0.1, 0.126, 0.158, 0.200, 0.251, 0.316, 0.398, 0.501, 0.631, 0.794, 1, 1.259, 1.585, 1.995, 2.512, 3.162, 3.981, 5.012, 6.310, 7.943, 10, \text{ and } 12.589 \text{ Gyr}$ ). The accretion disc (FC) is described as a power law of the form  $F_{\lambda} \propto \lambda^{-\alpha}$  (we used  $\alpha = 0.25, 0.5, \text{ and } 0.75$ ). Hot dust emission components are described as eight Planck distributions (black-body, BB), with temperature ranging from 700 K to 1400 K, in steps of 100 K. For display purposes on the bottom plot we zoom in the SSPs. The identification of the components are on the labels. For details see the text.

*xi*: sum of the per cent contribution of SSPs with ages in the range  $100 \text{ Myr} < t \leq 700 \text{ Myr}$ . This represents the peak of the Balmer absorption lines.

*xio*: sum of the per cent contribution SSPs with ages in the range  $700 \text{ Myr} < t \leq 2 \text{ Gyr}$ . Being the representative of the AGB peak contribution.

*xo*: sum of the per cent contribution  $2 \text{ Gyr} < t \leq 13 \text{ Gyr}$ . Represents the older underlying population.

HD: sum of the per cent contribution of all Planck function components, representing hot dust emission.

FC: sum of the per cent contribution of all power-law featureless components, representing the AGN accretion disc contribution.

If limited to selecting only two parameters to describe the stellar population composition of a galaxy, the optimal choice would undoubtedly be its mean age and mean-metallicity. Therefore, we have followed Cid Fernandes et al. (2005) and computed the mean ages (the logarithm of the age, actually) for each galaxy weighted by the stellar light

$$\langle \log t_{\star} \rangle_L = \sum_{j=1}^{N_{\star}} x_j \log t_j, \quad (3)$$

and weighted by the stellar mass,

$$\langle \log t_{\star} \rangle_M = \sum_{j=1}^{N_{\star}} \mu_j \log t_j. \quad (4)$$

Subsequently, we convert these quantities into ages in Gyr (e.g. removing the logarithmic scale).

The light-weighted mean metallicity is defined as

$$\langle Z_{\star} \rangle_L = \sum_{j=1}^{N_{\star}} x_j Z_j, \quad (5)$$

and the mass-weighted mean metallicity is defined by:

$$\langle Z_{\star} \rangle_M = \sum_{j=1}^{N_{\star}} \mu_j Z_j. \quad (6)$$

Note that all these values are limited by the elements included in the base. In principle, the mass-weighted properties are more physical, but, since the stellar  $M/L$  is non-constant, they have a much less direct relation with the observed spectrum than the light-weighted ones. For more details see Cid Fernandes et al. (2005).

Besides the actual stellar mass of the galaxy<sup>4</sup> ( $M_{\star}$ ), STARLIGHT also outputs the mass that has been processed into stars throughout the galaxy's life ( $M_{\star}^{\text{ini}}$ ). Using this, one can compute the mass that has returned to the interstellar medium, as  $M_{\star}^{\text{Ret}} = M_{\star}^{\text{ini}} - M_{\star}$ . These quantities are listed in Table 3.

Finally, these quantities have been derived as the mean value of all the fitting on the simulated spectra with the uncertainty being its standard deviation (see Section 3.1).

## 4.2 Stellar population properties

In Fig. 4 we show the distribution (mean and median values are also shown) of the results of the 100 simulated spectra for each galaxy (see Section 3.1) for the binned population vectors as well as for mean ages and metallicities for the AGN hosts (blue) and control galaxies (red). The mean values and their standard deviations are summarized in Table 3.

The stellar populations, using the UV/Optical arms of X-shooter spectra, of part of the present sample (mostly Sy 2 sources) of LLAMA AGN have been studied by Burtcher et al. (2021); however, using the Bruzual & Charlot (2003) SSP models, including ages younger than 50 Myr in the base of elements. Aiming to compare the optical and NIR stellar population results fairly, we have fitted the X-shooter UV/Optical<sup>5</sup> using the same approach as used for the

<sup>4</sup>Note that this is the mass inside the aperture size, see Section 4.2.5 for a discussion.

<sup>5</sup>From 3850 Å to 8800 Å with  $\lambda_{\text{norm}} = 6840 \text{ Å}$ .

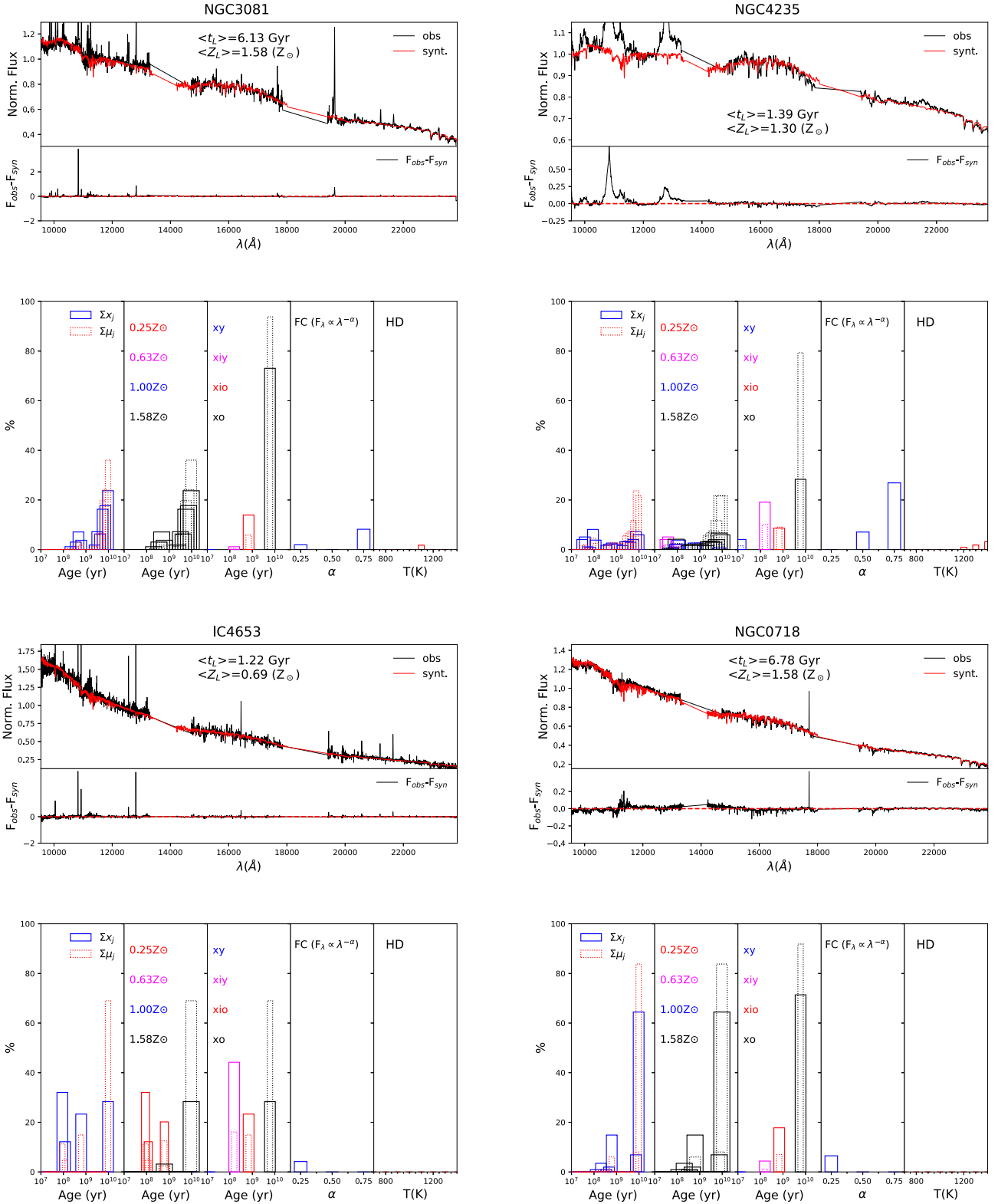


**Figure 3.** Spectral fitting results for NGC 3081 (AGN, Sy 2), NGC 4235 (AGN, Sy 1), IC 4653 (CNT, star-forming) and NGC 0718 (CNT, passive) for the original spectrum (e.g. without the perturbations described in Section 3.1). For each galaxy, on *top panel*: observed (black) and synthetic (red) spectra, light-weighted mean age, and metallicity. *middle panel*: emission-line free spectrum (observed–synthetic spectrum) and a horizontal line showing the zero point for the continuum. *bottom panel*: from left to right, SFH summed over all metallicities in light ( $x$ ) and in mass ( $\mu$ ) fractions; SFH considering different metallicities (they are labelled); binned population vectors; AGN feature-less continuum and hot-dust contributions are on the two last panels. The plots for the remaining sources are shown in on-line material.



**Table 3.** Properties obtained fitting the NIR spectral range.

Source	xy (per cent)	xy (per cent)	xio (per cent)	xio (per cent)	yo (per cent)	yo (per cent)	$\mu y$ (per cent)	$\mu y$ (per cent)	$\mu i y$ (per cent)	$\mu i y$ (per cent)	$\mu i o$ (per cent)	$\mu i o$ (per cent)	FC (per cent)	HD (per cent)	$<t > L$ (Gyr)	$<t > M$ (Gyr)	$<Z > L$ ( $Z_{\odot}$ )	$<Z > L$ ( $Z_{\odot}$ )	$\log M_{\star}$ ( $M_{\odot}$ )	$\log M_{\star}^{\text{ret}}$ ( $M_{\odot}$ )	Av (mag)	$\chi^2_{\text{red}}$
ESO21-G004	7 ± 1	5 ± 2	0 ± 0	88 ± 1	1 ± 0	1 ± 0	1 ± 0	1 ± 0	1 ± 0	1 ± 0	99 ± 0	1 ± 0	1 ± 0	0 ± 0	7.26 ± 0.39	11.80 ± 0.11	1.48 ± 0.01	1.57 ± 0.00	9.96 ± 0.56	10.00 ± 0.54	0.02 ± 0.02	8 ± 0
ESO137-G034	0 ± 0	33 ± 0	10 ± 1	51 ± 0	0 ± 0	8 ± 0	0 ± 0	0 ± 0	8 ± 0	6 ± 0	86 ± 0	5 ± 0	0 ± 0	0 ± 0	2.57 ± 0.04	8.08 ± 0.08	1.12 ± 0.01	1.47 ± 0.00	9.04 ± 0.60	9.05 ± 0.57	-1.00 ± 0.00	7 ± 0
MCG-05-14-012	1 ± 3	0 ± 1	6 ± 8	32 ± 7	0 ± 1	0 ± 1	9 ± 12	91 ± 12	61 ± 4	0 ± 0	6.25 ± 2.66	7.58 ± 2.26	0.84 ± 0.43	0 ± 0	6.25 ± 2.66	7.58 ± 2.26	0.84 ± 0.43	0.81 ± 0.45	8.40 ± 0.48	8.43 ± 0.45	-0.00 ± 0.15	1 ± 0
MCG-05-23-016	0 ± 0	1 ± 2	10 ± 5	21 ± 4	0 ± 0	1 ± 2	14 ± 9	85 ± 9	68 ± 2	0 ± 0	4.78 ± 1.45	7.02 ± 1.23	1.56 ± 0.04	0 ± 0	4.78 ± 1.45	7.02 ± 1.23	1.56 ± 0.04	1.57 ± 0.02	8.90 ± 0.46	8.90 ± 0.46	0.03 ± 0.08	1 ± 0
MCG-06-30-015	0 ± 0	7 ± 2	8 ± 2	31 ± 5	0 ± 0	6 ± 2	8 ± 3	87 ± 4	50 ± 2	5 ± 0	3.31 ± 0.53	5.76 ± 0.38	1.28 ± 0.04	0 ± 0	3.31 ± 0.53	5.76 ± 0.38	1.28 ± 0.04	1.41 ± 0.03	8.81 ± 0.48	8.78 ± 0.46	0.83 ± 0.04	11 ± 0
NGC1365	0 ± 0	0 ± 0	0 ± 0	21 ± 1	0 ± 0	0 ± 0	0 ± 0	100 ± 0	76 ± 1	2 ± 0	9.95 ± 0.66	10.40 ± 0.50	1.25 ± 0.04	0 ± 0	9.95 ± 0.66	10.40 ± 0.50	1.25 ± 0.04	1.26 ± 0.04	8.65 ± 0.52	8.68 ± 0.49	1.29 ± 0.06	11 ± 0
NGC2110	0 ± 0	2 ± 1	10 ± 2	41 ± 1	0 ± 0	1 ± 1	7 ± 1	92 ± 1	47 ± 1	0 ± 0	5.20 ± 0.26	7.70 ± 0.29	1.58 ± 0.00	0 ± 0	5.20 ± 0.26	7.70 ± 0.29	1.58 ± 0.00	1.58 ± 0.00	9.42 ± 0.52	9.42 ± 0.50	0.83 ± 0.03	2 ± 0
NGC2992	2 ± 2	2 ± 1	0 ± 0	69 ± 2	0 ± 0	0 ± 0	0 ± 0	99 ± 0	19 ± 1	8 ± 1	8.33 ± 0.91	10.70 ± 0.24	1.26 ± 0.03	0 ± 0	8.33 ± 0.91	10.70 ± 0.24	1.26 ± 0.03	1.30 ± 0.02	9.73 ± 0.51	9.76 ± 0.49	1.01 ± 0.09	16 ± 0
NGC3081	0 ± 0	2 ± 3	16 ± 4	62 ± 11	0 ± 0	1 ± 1	8 ± 3	91 ± 3	18 ± 7	1 ± 1	5.20 ± 0.95	7.71 ± 0.56	1.58 ± 0.00	0 ± 0	5.20 ± 0.95	7.71 ± 0.56	1.58 ± 0.00	1.58 ± 0.00	9.20 ± 0.48	9.20 ± 0.46	0.53 ± 0.10	8 ± 0
NGC3783	3 ± 2	10 ± 3	8 ± 2	25 ± 5	1 ± 1	8 ± 4	9 ± 5	82 ± 8	47 ± 3	7 ± 0	2.29 ± 0.52	5.72 ± 0.76	0.82 ± 0.06	0 ± 0	2.29 ± 0.52	5.72 ± 0.76	0.82 ± 0.06	0.99 ± 0.05	9.17 ± 0.48	9.15 ± 0.46	-0.28 ± 0.06	18 ± 0
NGC4235	2 ± 2	24 ± 7	8 ± 6	26 ± 6	1 ± 1	15 ± 6	10 ± 8	74 ± 10	34 ± 3	6 ± 1	1.38 ± 0.51	4.28 ± 1.10	1.31 ± 0.10	0 ± 0	1.38 ± 0.51	4.28 ± 1.10	1.31 ± 0.10	1.46 ± 0.06	8.98 ± 0.48	8.93 ± 0.45	1.78 ± 0.17	1 ± 0
NGC4388	0 ± 0	6 ± 2	0 ± 0	74 ± 4	0 ± 0	2 ± 1	0 ± 0	98 ± 1	16 ± 2	5 ± 0	6.60 ± 0.50	8.29 ± 0.29	1.58 ± 0.00	0 ± 0	6.60 ± 0.50	8.29 ± 0.29	1.58 ± 0.00	1.58 ± 0.00	9.25 ± 0.50	9.25 ± 0.48	2.45 ± 0.03	8 ± 0
NGC4593	7 ± 2	1 ± 2	0 ± 0	28 ± 5	3 ± 2	0 ± 1	0 ± 0	100 ± 0	0 ± 0	0 ± 0	3.36 ± 1.22	8.27 ± 0.89	0.62 ± 0.05	0 ± 0	3.36 ± 1.22	8.27 ± 0.89	0.62 ± 0.05	0.74 ± 0.07	8.74 ± 0.48	8.77 ± 0.46	0.59 ± 0.15	12 ± 0
NGC5128	0 ± 0	0 ± 0	0 ± 0	100 ± 0	0 ± 0	0 ± 0	0 ± 0	100 ± 0	0 ± 0	0 ± 0	8.40 ± 0.19	9.47 ± 0.14	1.58 ± 0.00	0 ± 0	8.40 ± 0.19	9.47 ± 0.14	1.58 ± 0.00	1.58 ± 0.00	8.26 ± 0.56	8.27 ± 0.53	3.18 ± 0.00	17 ± 0
NGC5506	8 ± 4	1 ± 2	14 ± 6	24 ± 9	5 ± 4	1 ± 3	27 ± 16	66 ± 19	30 ± 3	23 ± 2	1.53 ± 0.73	2.75 ± 0.95	1.04 ± 0.14	0 ± 0	1.53 ± 0.73	2.75 ± 0.95	1.04 ± 0.14	1.01 ± 0.14	9.37 ± 0.46	9.27 ± 0.44	4.97 ± 0.15	1 ± 0
NGC5728	0 ± 0	0 ± 3	38 ± 5	55 ± 3	0 ± 0	0 ± 1	18 ± 3	82 ± 2	7 ± 2	0 ± 0	4.70 ± 0.40	7.80 ± 0.39	0.48 ± 0.08	0 ± 0	4.70 ± 0.40	7.80 ± 0.39	0.48 ± 0.08	0.59 ± 0.10	9.21 ± 0.51	9.24 ± 0.48	1.31 ± 0.16	25 ± 6
NGC6814	0 ± 1	23 ± 3	0 ± 0	47 ± 3	0 ± 0	7 ± 1	0 ± 0	93 ± 1	26 ± 1	4 ± 1	2.94 ± 0.33	8.20 ± 0.33	1.21 ± 0.03	0 ± 0	2.94 ± 0.33	8.20 ± 0.33	1.21 ± 0.03	1.37 ± 0.02	8.87 ± 0.52	8.88 ± 0.49	0.85 ± 0.07	10 ± 0
NGC7172	1 ± 2	18 ± 5	27 ± 5	15 ± 4	0 ± 1	17 ± 5	35 ± 8	48 ± 9	5 ± 2	34 ± 1	1.25 ± 0.24	2.34 ± 0.56	1.22 ± 0.07	0 ± 0	1.25 ± 0.24	2.34 ± 0.56	1.22 ± 0.07	1.31 ± 0.06	8.77 ± 0.49	8.65 ± 0.46	0.87 ± 0.12	14 ± 0
NGC7213	0 ± 0	13 ± 6	10 ± 6	38 ± 7	0 ± 0	7 ± 3	7 ± 10	86 ± 9	39 ± 4	0 ± 0	3.75 ± 0.86	7.29 ± 0.92	1.43 ± 0.13	0 ± 0	3.75 ± 0.86	7.29 ± 0.92	1.43 ± 0.13	1.53 ± 0.13	9.17 ± 0.49	9.16 ± 0.46	0.36 ± 0.08	1 ± 0
NGC7582	0 ± 0	2 ± 1	12 ± 2	54 ± 4	0 ± 0	1 ± 0	6 ± 1	93 ± 1	27 ± 2	6 ± 0	6.34 ± 0.46	8.84 ± 0.27	1.33 ± 0.05	0 ± 0	6.34 ± 0.46	8.84 ± 0.27	1.33 ± 0.05	1.50 ± 0.02	9.16 ± 0.49	9.17 ± 0.47	1.86 ± 0.06	7 ± 0
ESO093-G003	0 ± 0	18 ± 2	3 ± 1	75 ± 1	0 ± 0	3 ± 0	1 ± 0	96 ± 0	4 ± 0	0 ± 0	5.02 ± 0.37	10.30 ± 0.20	1.54 ± 0.02	0 ± 0	5.02 ± 0.37	10.30 ± 0.20	1.54 ± 0.02	1.58 ± 0.00	9.03 ± 0.55	9.06 ± 0.53	-0.25 ± 0.02	5 ± 0
ESO208-G021	0 ± 0	0 ± 0	0 ± 0	100 ± 0	0 ± 0	0 ± 0	0 ± 0	100 ± 0	0 ± 0	0 ± 0	9.21 ± 0.90	9.46 ± 0.67	1.58 ± 0.00	0 ± 0	9.21 ± 0.90	9.46 ± 0.67	1.58 ± 0.00	1.58 ± 0.00	9.29 ± 0.50	9.30 ± 0.48	0.35 ± 0.01	1 ± 0
IC4653	0 ± 0	44 ± 1	23 ± 2	28 ± 1	0 ± 0	16 ± 0	15 ± 1	69 ± 1	4 ± 0	0 ± 0	1.22 ± 0.02	4.82 ± 0.11	0.69 ± 0.01	0 ± 0	1.22 ± 0.02	4.82 ± 0.11	0.69 ± 0.01	1.20 ± 0.01	8.13 ± 0.58	8.10 ± 0.54	-1.00 ± 0.00	3 ± 0
NGC0718	0 ± 0	5 ± 1	16 ± 1	72 ± 1	0 ± 0	1 ± 0	6 ± 0	92 ± 0	7 ± 0	0 ± 0	6.92 ± 0.11	10.20 ± 0.13	1.58 ± 0.00	0 ± 0	6.92 ± 0.11	10.20 ± 0.13	1.58 ± 0.00	1.58 ± 0.00	8.91 ± 0.59	8.94 ± 0.55	-0.27 ± 0.01	16 ± 0
NGC1079	9 ± 12	19 ± 17	2 ± 5	65 ± 16	1 ± 2	6 ± 7	1 ± 2	92 ± 7	5 ± 3	0 ± 0	4.29 ± 2.78	8.70 ± 2.23	1.39 ± 0.19	0 ± 0	4.29 ± 2.78	8.70 ± 2.23	1.39 ± 0.19	1.50 ± 0.14	8.75 ± 0.48	8.77 ± 0.45	1.33 ± 0.24	1 ± 0
NGC1315	0 ± 0	0 ± 0	12 ± 2	88 ± 2	0 ± 0	0 ± 0	4 ± 1	96 ± 1	0 ± 0	0 ± 0	9.20 ± 0.46	11.50 ± 0.20	1.58 ± 0.02	0 ± 0	9.20 ± 0.46	11.50 ± 0.20	1.58 ± 0.02	1.58 ± 0.02	8.39 ± 0.56	8.43 ± 0.53	-0.40 ± 0.02	1 ± 0
NGC1947	0 ± 2	7 ± 6	3 ± 4	90 ± 5	0 ± 0	2 ± 2	1 ± 1	97 ± 1	0 ± 0	0 ± 0	6.51 ± 0.91	8.29 ± 1.14	1.57 ± 0.03	0 ± 0	6.51 ± 0.91	8.29 ± 1.14	1.57 ± 0.03	1.58 ± 0.01	8.84 ± 0.51	8.84 ± 0.48	0.90 ± 0.05	1 ± 0
NGC2775	0 ± 0	0 ± 0	17 ± 1	83 ± 1	0 ± 0	0 ± 0	6 ± 0	94 ± 0	0 ± 0	0 ± 0	6.39 ± 0.09	8.01 ± 0.12	1.58 ± 0.00	0 ± 0	6.39 ± 0.09	8.01 ± 0.12	1.58 ± 0.00	1.58 ± 0.00	9.43 ± 0.56	9.43 ± 0.53	0.24 ± 0.01	10 ± 0
NGC3175	0 ± 0	14 ± 0	0 ± 0	75 ± 0	0 ± 0	4 ± 0	0 ± 0	96 ± 0	10 ± 0	0 ± 0	7.70 ± 0.12	11.00 ± 0.10	1.57 ± 0.00	0 ± 0	7.70 ± 0.12	11.00 ± 0.10	1.57 ± 0.00	1.58 ± 0.00	8.32 ± 0.61	8.36 ± 0.57	1.63 ± 0.01	7 ± 0
NGC3351	0 ± 0	0 ± 0	8 ± 1	90 ± 1	0 ± 0	0 ± 0	3 ± 0	97 ± 0	1 ± 0	0 ± 0	10.10 ± 0.14	11.60 ± 0.13	1.58 ± 0.00	0 ± 0	10.10 ± 0.14	11.60 ± 0.13	1.58 ± 0.00	1.58 ± 0.00	8.48 ± 0.60	8.51 ± 0.56	0.81 ± 0.01	6 ± 0
NGC3717	0 ± 0	25 ± 1	0 ± 0	72 ± 1	0 ± 0	4 ± 0	0 ± 0	96 ± 0	1 ± 1	2 ± 0	3.99 ± 0.14	10.20 ± 0.15	1.58 ± 0.00	0 ± 0	3.99 ± 0.14	10.20 ± 0.15	1.58 ± 0.00	1.58 ± 0.00	9.25 ± 0.55	9.28 ± 0.52	2.58 ± 0.02	6 ± 0
NGC3749	0 ± 0	0 ± 0	0 ± 0	92 ± 0	0 ± 0	0 ± 0	0 ± 0	100 ± 0	8 ± 0	0 ± 0	12.60 ± 0.04	12.60 ± 0.04	1.58 ± 0.00	0 ± 0	12.60 ± 0.04	12.60 ± 0.04	1.58 ± 0.00	1.58 ± 0.00	9.92 ± 0.61	9.96 ± 0.58	1.85 ± 0.00	16 ± 0
NGC4224	0 ± 0	23 ± 2	0 ± 0	77 ± 2	0 ± 0	3 ± 0	0 ± 0	97 ± 0	0 ± 0	0 ± 0	4.69 ± 0.47	10.80 ± 0.22	1.46 ± 0.02	0 ± 0	4.69 ± 0.47	10.80 ± 0.22	1.46 ± 0.02	1.57 ± 0.00	9.31 ± 0.54	9.34 ± 0.51	-0.01 ± 0.03	2 ± 0
NGC4254	0 ± 0	25 ± 1	1 ± 0	74 ± 0	0 ± 0	6 ± 0	0 ± 0	94 ± 0	2 ± 0	0 ± 0	5.40 ± 0.10	9.89 ± 0.13	1.51 ± 0.01	0 ± 0	5.40 ± 0.10	9.89 ± 0.13	1.51 ± 0.01	1.57 ± 0.00	8.39 ± 0.60	8.41 ± 0.56	0.50 ± 0.01	5 ± 0
NGC4260	0 ± 0	0 ± 0	0 ± 0	21 ± 1	0 ± 0	0 ± 0	8 ± 0	92 ± 0	0 ± 0	0 ± 0	6.94 ± 0.10	9.03 ± 0.20	1.53 ± 0.01	0 ± 0	6.94 ± 0.10	9.03 ± 0.20	1.53 ± 0.01	1.53 ± 0.01	8.82 ± 0.57	8.84 ± 0.53	0.28 ± 0.01	5 ± 0
NGC5037	0 ± 0	0 ± 0	0 ± 0	94 ± 0	0 ± 0	0 ± 0	0 ± 0	100 ± 0	6 ± 0	0 ± 0	12.60 ± 0.03	12.60 ± 0.00	1.42 ± 0.02	0 ± 0	12.60 ± 0.03	12.60 ± 0.00	1.42 ± 0.02	1.42 ± 0.02	9.11 ± 0.59	9.15 ± 0.58	0.65 ± 0.01	3 ± 0
NGC5845	0 ± 0	0 ± 0	4 ± 0	96 ± 0	0 ± 0	1 ± 0	99 ± 0	0 ± 0	0 ± 0	0 ± 0	11.40 ± 0.14	12.30 ± 0.11	1.42 ± 0.02	0 ± 0	11.40 ± 0.14	12.30 ± 0.11	1.42 ± 0.02	1.44 ± 0.02	9.43 ± 0.59	9.47 ± 0.56	0.30 ± 0.01	39 ± 0
NGC5921	0 ± 0	12 ± 1	5 ± 1	79 ± 1	0 ± 0	3 ± 0	2 ± 0	95 ± 0	4 ± 0	0 ± 0	6.45 ± 0.07	9.54 ± 0.17	1.58 ± 0.00	0 ± 0	6.45 ± 0.07	9.54 ± 0.17	1.58 ± 0.00	1.58 ± 0.00	9.94 ± 0.56	9.95 ± 0.52	0.04 ± 0.01	18 ± 0
NGC7727	0 ± 0	0 ± 0	0 ± 0	97 ± 0	0 ± 0	0 ± 0	0 ± 0	100 ± 0	3 ± 0	0 ± 0	12.60 ± 0.00	12.60 ± 0.00	1.58 ± 0.00	0 ± 0	12.60 ± 0.00	12.60 ± 0.00	1.58 ± 0.00	1.58 ± 0.00	9.49 ± 0.69			

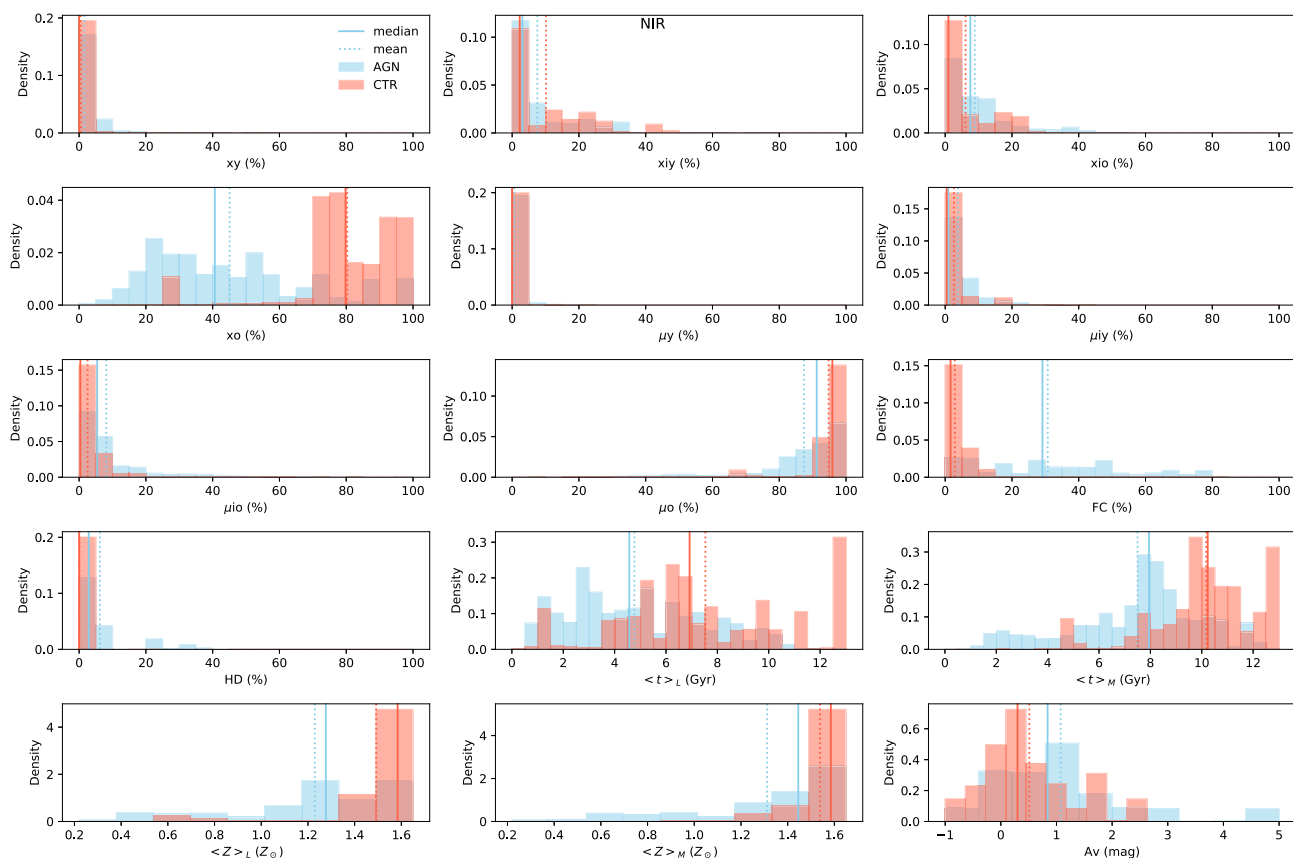


**Figure 4.** Mean stellar population properties of the sample obtained after fitting the 100 simulated spectra (see Section 3.1). In blue AGN hosts and red control galaxies. Mean (dotted line) and median (full line) are shown. Population vectors are defined as follows:  $xy \leq 100$  Myr,  $100 \text{ Myr} < xiy \leq 700$  Myr,  $700 \text{ Gyr} < xio \leq 2$  Gyr, and  $2 \text{ Gyr} < xyo \leq 13$  Gyr. HD and FC are the sum of the percent contribution of the Planck function and the power-law featureless components, respectively. Mean age and metallicities are defined according to equations (3), (4), (5), and (6). The mean values and their standard deviations are listed in Table 3.

NIR spectral range described above. The results of these fittings are shown in Fig. 5 and summarized in Table 4. It is also worth mentioning that the results obtained by Burtcher et al. (2021) using the Bruzual & Charlot (2003) models are in good agreement with those found here when fitting the X-shooter data with the XSL models (see Section 4.2.5 for a comparison on the derived stellar masses).

#### 4.2.1 Optical versus NIR fits

The results of our optical and NIR fits are in very good agreement (Figs 5 and 6) in terms of the stellar population ages. The main difference between optical and NIR results is in the metallicities and FC components.

The NIR fits, in general, show higher metallicities than the optical ones, especially when looking at the control galaxies. The optical results show small differences in  $Z$  between controls and AGN with both samples spanning a large range of metallicities (on average AGN presents a slightly higher metallicity than controls). On the other hand, the NIR fits do show a larger difference between mean metallicities in both samples. We attribute this difference to the fact that the optical spectral range has more features sensitive to metallicity than the NIR window and/or to the higher SNR of the optical data when compared with the NIR ones. Regarding the FC components in the NIR, we see a tail towards a larger fraction in the distribution of FC fractions in AGN when compared with the optical results. This may be related to the degeneracy between the FC and

HD components (see Riffel et al. 2022, for details). Finally, it is worth mentioning that in the NIR we can fit also the type 1 sources.

#### 4.2.2 Stellar population components

What emerges from this is that the AGN hosts have larger fractions of intermediate-age, less metallic stellar populations when compared with the control sample. Additionally, the AGN show higher reddening and, as expected only they require significant fractions of FC and HD components to fit their underlying spectrum.

In Burtcher et al. (2021) we have shown that the LLAMA AGN show, in general, a recent cessation of their star formation, i.e. it happened at least 6 Myr ago. We cannot examine this here because of the very young age limitations in our base (see Section 3), but in the younger stellar populations bin, we do not see any significant difference in both samples, with AGN exhibiting only a slightly higher mean value for  $xy$ .

Our results (Fig. 4) show that AGN present a lower fraction of the old stellar population when compared with controls ( $\mu o$  panel). The lower  $\mu o$  fractions are therefore compensated by the higher fraction of younger stellar populations<sup>6</sup> (e.g. one fraction comes

<sup>6</sup>Note that in the case of the light-weighted fractions, where the difference between the AGN and controls are even more pronounced, one has to have in mind that besides the SSP components the FC and HD also contribute, however, they have no contribution in the stellar mass fraction.

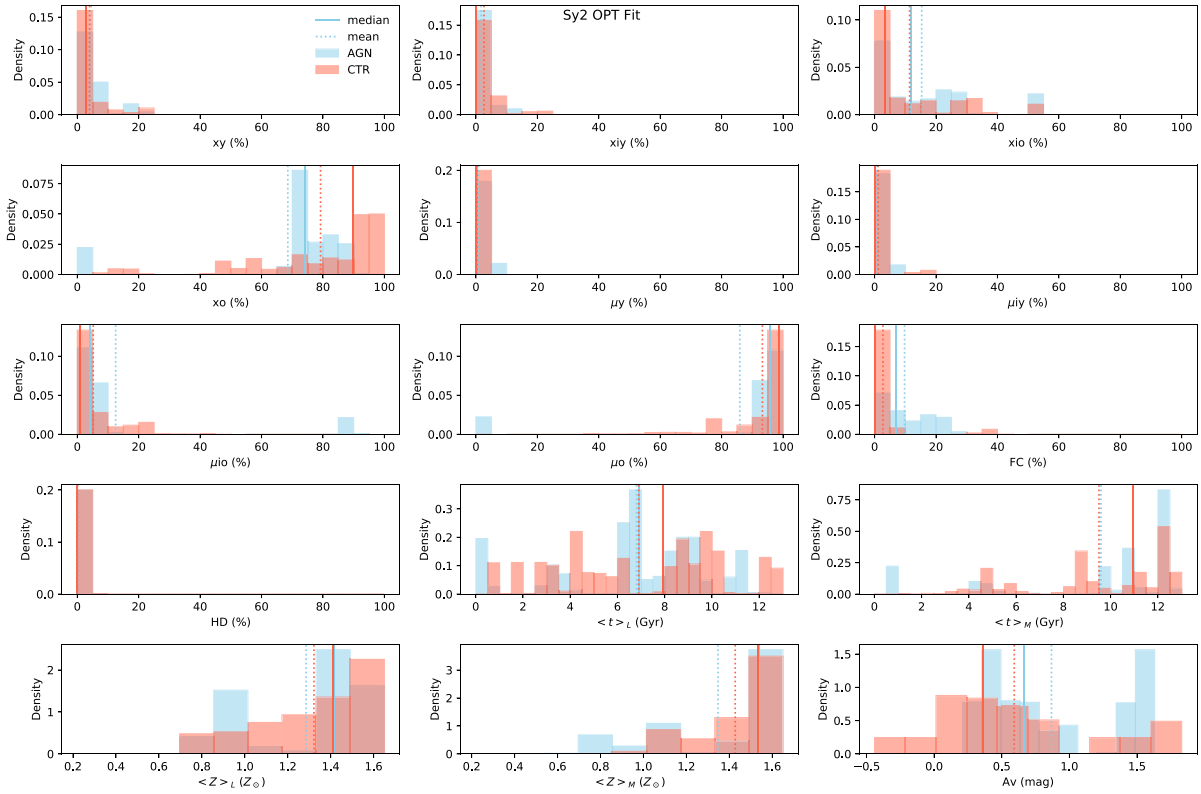


**Figure 5.** Mean stellar population properties of the Sy 2 sample obtained after fitting UV/Optical spectral region of the 100 simulated spectra (see Section 3.1). In blue AGN hosts and red control galaxies. The mean (dotted line) and the median (full line) values are shown.

down, the other has to go up), thus, AGN present larger fractions of intermediate-age populations when compared with the control sources. This is directly reflected in the  $\langle t \rangle_L$  mean/median values (4.7/4.5 Gyr for AGN and 7.5/6.9 Gyr for the controls) as well as in the  $\langle t \rangle_M$  mean/median values (7.5/8.0 Gyr for AGN and 10.2/10.2 Gyr for the controls).

Based on high angular resolution integral field observations, Riffel et al. (2022) found that the inner region ( $R \lesssim 125$  pc) of AGN is primarily composed of intermediate-age SP (with an average age  $\langle t \rangle_L \lesssim 1.5$  Gyr). They also observed a correlation between the bolometric luminosity of AGN and the mean age of their stellar populations, indicating that more luminous AGN tend to have larger amounts of intermediate-age stars. This has been interpreted as suggesting a delay between the formation of new stars and the triggering/feeding of the AGN. In this sense, these intermediate-age stars contribute to the gas supply around the supermassive black hole through mass-loss during stellar evolution. This gas, which has a low velocity (a few hundred  $\text{km s}^{-1}$ ), combines with the existing gas which is flowing towards the central region of the host galaxy (e.g. Cuadra et al. 2006; Fathi et al. 2006; Davies et al. 2007; Riffel et al. 2008a, 2022, 2023b; Müller Sánchez et al. 2009; Riffel, Storch-Bergmann & Winge 2013b; Audibert et al. 2019; Diniz et al. 2019; Storch-Bergmann & Schnorr-Müller 2019; Audibert et al. 2021) and feeding the SMBH.

Furthermore, studies have detected young to intermediate-age populations in the inner regions of AGN host galaxies (e.g. Oliva et al. 1995; González Delgado, Heckman & Leitherer 2001; Imanishi & Wada 2004; Davies et al. 2005, 2007; Riffel et al. 2007, 2009, 2010, 2011a, 2015, 2022, 2023b; Storch-Bergmann et al. 2012; Diniz et al. 2017; Mallmann et al. 2018; de Lorenzo-Cáceres et al. 2020;

Burtscher et al. 2021; Salvador-Rusiñol et al. 2021; Dahmer-Hahn et al. 2022). These populations are predominantly composed of short-lived stars ( $t \simeq 0.2 - 2$  Gyr;  $M \simeq 2 - 6 M_{\odot}$ ) that release significant amounts of material into the nuclear environment (from  $\sim 30$  per cent–80 per cent of their masses; Bertolami 2016). This material can fuel the SMBH with additional gas, thereby enhancing AGN brightness or triggering its activity or alternatively, it can cool down and form new stars (e.g. de Lorenzo-Cáceres et al. 2020; Salvador-Rusiñol et al. 2020, 2021; Benedetti et al. 2023).

#### 4.2.3 The FC and HD components

As can be seen in Table 3 the FC component is required to fit the spectral energy distribution of almost all the AGNs, being the only exception NGC 5128. This component is also required in 63 per cent (12/19 sources) to fit the control galaxies, with a maximum contribution of 10 per cent. The degeneracy of the FC and a young stellar population is a well-known and common problem in the study of the stellar content of active galaxies (e.g. Koski 1978; Cid Fernandes et al. 2004, 2005; Riffel et al. 2009, and references therein). This degeneracy is due to the fact that the continuum of a reddened young starburst ( $t \lesssim 5$  Myr) is indistinguishable from an AGN-type continuum. In the optical, broad components in polarized light of Sy 2 galaxies only show up when this component is larger than  $\sim 20$  per cent (Cid Fernandes & Terlevich 1995). Taking our results into account, one could say that in the NIR the young and FC components can be separated for values larger than 10 per cent (the maximum value reached in the control sample). Thus, for four AGN (ESO021-G004, ESO137-G034, NGC5728, and NGC 7172) the FC component could not be distinguished from a young

**Table 4.** Properties obtained fitting the optical spectral range for the galaxies studied in Burtcher et al. (2021).

Source	xy (per cent)	x <sub>1y</sub> (per cent)	x <sub>10</sub> (per cent)	x <sub>0</sub> (per cent)	μ <sub>y</sub> (per cent)	μ <sub>iy</sub> (per cent)	μ <sub>io</sub> (per cent)	μ <sub>o</sub> (per cent)	FC (per cent)	HD (per cent)	<t>L (Gyr)	<t>M (Gyr)	<Z>L (Z <sub>⊙</sub> )	<Z>L (Z <sub>⊙</sub> )	logM <sub>*</sub> (M <sub>⊙</sub> )	logM <sub>*</sub> <sup>Ret</sup> (M <sub>⊙</sub> )	A <sub>v</sub> (mag)	χ <sub>red</sub> <sup>2</sup>
NGC2110	6 ± 1	0 ± 0	0 ± 0	71 ± 1	0 ± 0	0 ± 0	0 ± 0	100 ± 0	24 ± 2	0 ± 0	8.38 ± 0.38	12.30 ± 0.04	0.02 ± 0.00	0.02 ± 0.00	8.97 ± 0.53	9.01 ± 0.50	0.56 ± 0.01	1 ± 0
NGC2992	0 ± 0	0 ± 0	5 ± 1	89 ± 0	0 ± 0	0 ± 0	1 ± 0	99 ± 0	6 ± 1	0 ± 0	11.20 ± 0.23	12.30 ± 0.04	0.02 ± 0.00	0.01 ± 0.00	9.25 ± 0.58	9.31 ± 0.56	1.61 ± 0.01	2 ± 0
MCG-05-23-016	9 ± 1	0 ± 0	0 ± 0	74 ± 1	0 ± 0	0 ± 0	0 ± 0	100 ± 0	16 ± 1	1 ± 0	6.81 ± 0.23	12.10 ± 0.16	0.02 ± 0.00	0.02 ± 0.00	8.71 ± 0.56	8.75 ± 0.53	0.66 ± 0.02	2 ± 0
NGC3081	5 ± 0	0 ± 0	0 ± 0	81 ± 0	0 ± 0	0 ± 0	0 ± 0	100 ± 0	14 ± 1	0 ± 0	9.25 ± 0.23	12.30 ± 0.20	0.02 ± 0.00	0.02 ± 0.00	8.91 ± 0.58	8.95 ± 0.54	0.48 ± 0.01	2 ± 0
ESO21-G004	3 ± 3	2 ± 3	13 ± 6	81 ± 4	0 ± 0	0 ± 0	5 ± 3	94 ± 3	1 ± 2	0 ± 0	3.42 ± 0.44	4.67 ± 0.56	0.02 ± 0.00	0.02 ± 0.00	8.94 ± 0.50	8.89 ± 0.47	0.92 ± 0.04	1 ± 0
NGC5728	0 ± 0	0 ± 0	28 ± 1	72 ± 1	0 ± 0	0 ± 0	7 ± 0	93 ± 0	0 ± 0	0 ± 0	6.40 ± 0.12	9.84 ± 0.17	0.02 ± 0.00	0.02 ± 0.00	9.16 ± 0.55	9.18 ± 0.52	0.39 ± 0.01	2 ± 0
ESO137-G034	0 ± 0	0 ± 0	17 ± 3	77 ± 2	0 ± 0	0 ± 0	5 ± 1	95 ± 1	7 ± 2	0 ± 0	8.61 ± 0.49	10.90 ± 0.28	0.01 ± 0.00	0.02 ± 0.00	8.99 ± 0.55	9.03 ± 0.52	0.26 ± 0.02	2 ± 0
NGC7172	0 ± 0	4 ± 1	23 ± 2	73 ± 1	0 ± 0	0 ± 0	6 ± 0	94 ± 0	0 ± 0	0 ± 0	6.69 ± 0.14	11.00 ± 0.05	0.02 ± 0.00	0.02 ± 0.00	9.02 ± 0.56	9.05 ± 0.54	1.53 ± 0.01	2 ± 0
NGC7582	18 ± 2	9 ± 3	52 ± 1	0 ± 0	6 ± 1	6 ± 2	88 ± 1	0 ± 0	20 ± 1	0 ± 0	0.49 ± 0.02	0.94 ± 0.02	0.01 ± 0.00	0.01 ± 0.00	8.16 ± 0.56	7.92 ± 0.52	1.39 ± 0.02	3 ± 0
Control sample																		
ESO093-G003	4 ± 1	0 ± 1	0 ± 0	96 ± 1	0 ± 0	0 ± 0	0 ± 0	100 ± 0	0 ± 0	0 ± 0	4.90 ± 0.17	8.55 ± 0.29	0.01 ± 0.00	0.01 ± 0.00	8.72 ± 0.54	8.74 ± 0.51	0.76 ± 0.01	2 ± 0
ESO208-G021	5 ± 1	1 ± 1	0 ± 0	93 ± 0	0 ± 0	0 ± 0	0 ± 0	100 ± 0	0 ± 0	0 ± 0	8.95 ± 0.16	12.30 ± 0.00	0.02 ± 0.00	0.02 ± 0.00	8.35 ± 0.59	8.39 ± 0.56	0.68 ± 0.01	2 ± 0
IC4653	13 ± 3	20 ± 2	16 ± 6	14 ± 3	3 ± 1	16 ± 2	20 ± 9	62 ± 9	37 ± 2	0 ± 0	0.78 ± 0.09	3.81 ± 0.63	0.01 ± 0.00	0.02 ± 0.00	7.11 ± 0.51	7.05 ± 0.48	-0.38 ± 0.03	2 ± 0
NGC0718	0 ± 0	0 ± 0	18 ± 1	82 ± 1	0 ± 0	0 ± 0	10 ± 0	90 ± 0	0 ± 0	0 ± 0	4.36 ± 0.03	4.79 ± 0.03	0.02 ± 0.00	0.02 ± 0.00	8.85 ± 0.64	8.82 ± 0.58	0.53 ± 0.00	1 ± 0
NGC1079	4 ± 0	0 ± 0	4 ± 1	90 ± 1	0 ± 0	0 ± 0	1 ± 0	99 ± 0	2 ± 1	0 ± 0	8.40 ± 0.22	11.40 ± 0.14	0.02 ± 0.00	0.02 ± 0.00	8.54 ± 0.56	8.57 ± 0.53	0.25 ± 0.02	1 ± 0
NGC1315	4 ± 0	0 ± 0	0 ± 1	95 ± 0	0 ± 0	0 ± 0	0 ± 0	100 ± 0	0 ± 0	0 ± 0	9.42 ± 0.11	12.10 ± 0.16	0.02 ± 0.00	0.02 ± 0.00	8.32 ± 0.58	8.38 ± 0.55	0.20 ± 0.00	1 ± 0
NGC1947	5 ± 1	1 ± 1	6 ± 2	89 ± 1	0 ± 0	0 ± 0	1 ± 0	98 ± 0	0 ± 0	0 ± 0	8.44 ± 0.14	12.10 ± 0.12	0.02 ± 0.00	0.02 ± 0.00	8.32 ± 0.58	8.36 ± 0.55	1.43 ± 0.01	2 ± 0
NGC2775	0 ± 0	0 ± 0	0 ± 0	100 ± 0	0 ± 0	0 ± 0	0 ± 0	100 ± 0	0 ± 0	0 ± 0	12.50 ± 0.13	12.60 ± 0.00	0.02 ± 0.00	0.02 ± 0.00	8.42 ± 0.67	8.47 ± 0.63	0.19 ± 0.00	2 ± 0
NGC3175	22 ± 1	8 ± 2	0 ± 0	70 ± 1	2 ± 0	1 ± 0	0 ± 0	97 ± 0	0 ± 0	0 ± 0	1.83 ± 0.05	8.55 ± 0.16	0.02 ± 0.00	0.02 ± 0.00	7.99 ± 0.58	8.01 ± 0.54	1.21 ± 0.01	1 ± 0
NGC3351	1 ± 1	1 ± 1	10 ± 2	79 ± 1	0 ± 0	0 ± 0	3 ± 0	97 ± 0	7 ± 1	0 ± 0	5.72 ± 0.30	8.76 ± 0.36	0.02 ± 0.00	0.02 ± 0.00	7.28 ± 0.55	7.29 ± 0.52	0.52 ± 0.01	1 ± 0
NGC3717	1 ± 1	7 ± 2	32 ± 2	59 ± 1	0 ± 0	1 ± 0	10 ± 1	89 ± 1	0 ± 0	0 ± 0	4.34 ± 0.11	9.39 ± 0.16	0.02 ± 0.00	0.02 ± 0.00	8.59 ± 0.56	8.61 ± 0.53	1.65 ± 0.01	1 ± 0
NGC3749	0 ± 0	0 ± 0	27 ± 1	73 ± 1	0 ± 0	0 ± 0	8 ± 0	92 ± 0	0 ± 0	0 ± 0	6.09 ± 0.11	8.75 ± 0.10	0.02 ± 0.00	0.02 ± 0.00	9.20 ± 0.57	9.21 ± 0.54	1.82 ± 0.01	2 ± 0
NGC4224	0 ± 0	1 ± 0	4 ± 1	92 ± 1	0 ± 0	0 ± 0	1 ± 0	99 ± 0	2 ± 0	0 ± 0	9.91 ± 0.17	11.10 ± 0.12	0.02 ± 0.00	0.02 ± 0.00	9.18 ± 0.59	9.21 ± 0.55	0.35 ± 0.00	1 ± 0
NGC4254	0 ± 0	0 ± 0	53 ± 1	47 ± 1	0 ± 0	0 ± 0	22 ± 1	78 ± 1	0 ± 0	0 ± 0	3.43 ± 0.07	5.81 ± 0.16	0.02 ± 0.00	0.02 ± 0.00	8.45 ± 0.56	8.41 ± 0.52	0.28 ± 0.01	1 ± 0
NGC5037	3 ± 0	0 ± 0	0 ± 0	96 ± 1	0 ± 0	0 ± 0	0 ± 0	100 ± 0	1 ± 1	0 ± 0	9.97 ± 0.34	11.90 ± 0.26	0.02 ± 0.00	0.02 ± 0.00	8.54 ± 0.56	8.59 ± 0.53	0.89 ± 0.01	2 ± 0
NGC5845	2 ± 0	1 ± 1	2 ± 0	95 ± 0	0 ± 0	0 ± 0	0 ± 0	100 ± 0	0 ± 0	1 ± 0	10.30 ± 0.12	12.10 ± 0.15	0.02 ± 0.00	0.02 ± 0.00	8.87 ± 0.59	8.90 ± 0.55	0.03 ± 0.00	2 ± 0
NGC5921	5 ± 0	0 ± 0	1 ± 1	32 ± 3	2 ± 0	2 ± 0	18 ± 1	66 ± 2	0 ± 0	0 ± 0	2.59 ± 0.05	4.82 ± 0.15	0.02 ± 0.00	0.02 ± 0.00	8.61 ± 0.55	8.57 ± 0.52	0.29 ± 0.00	1 ± 0
NGC7727	0 ± 0	0 ± 0	0 ± 0	001 ± 0	0 ± 0	0 ± 0	100 ± 0	101 ± 0	0 ± 0	0 ± 0	12.30 ± 0.17	12.40 ± 0.19	0.02 ± 0.00	0.02 ± 0.00	8.87 ± 0.58	8.91 ± 0.54	-0.03 ± 0.01	1 ± 0



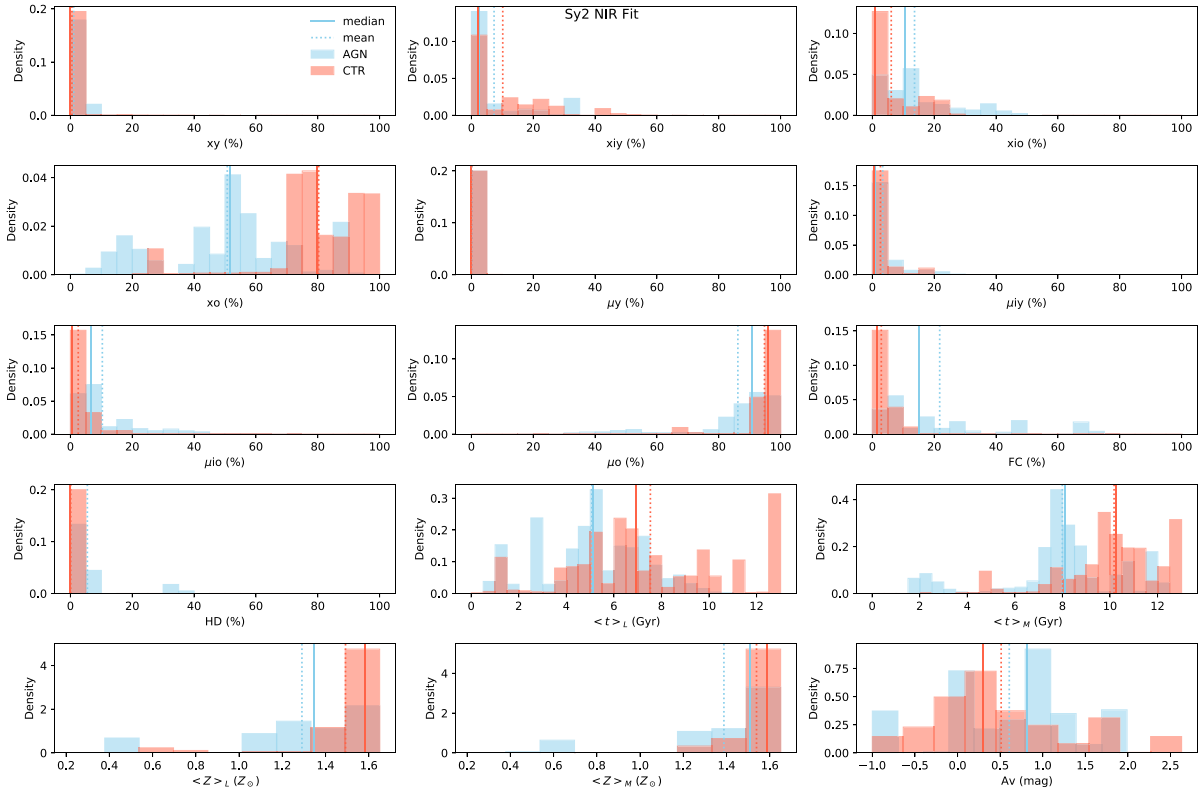


**Figure 6.** Same as Fig. 4, but for the NIR spectral region.

stellar population component. This is in agreement with the results presented in Riffel et al. (2022) who found that the FC can be associated with the accretion disc emission only for sources with  $FC \gtrsim 15$  percent.

The HD component is necessary to fit 60 percent (12/20) of the AGN, while it is only required in one of the control galaxies (NGC 3717), with a very low contribution (2 percent, within the uncertainties of our fits, see supplementary material). This component is very common in type 1 sources and is detected in around 50 per cent of type 2 sources (e.g. Riffel et al. 2006, 2009, 2010, 2022; Martins et al. 2010; Gaspar et al. 2019). For caveats on hot dust versus featureless continuum fitting see Riffel et al. (2022).

#### 4.2.4 Comparison of Seyfert 1 and Seyfert 2 fits

In Fig. 7 we compare the fitting results obtained for Sy 1 (green) and Sy 2 (yellow). In general, type 1 objects show higher fractions of  $xy$  and  $x_{iy}$  than the type 2 objects, while Sy 2 sources present higher fractions of the older populations ( $x_{io}$  and  $x_o$ ). In terms of mean ages, the Sy 1 galaxies display a mean value of  $\langle t \rangle \sim 3$  Gyr while the type 2 objects are characterized by slightly older mean ages ( $\langle t \rangle \sim 5$  Gyr). In terms of mass fractions, the mean values of all population vectors are quite similar. The same trend is also seen in the  $\langle t \rangle_M$  values. Both samples have similar reddening distributions with type 1 galaxies displaying a tail towards higher  $A_V$  values. In terms of the stellar metallicities, Sy 2 galaxies have slightly higher mean metallicities when compared with the Sy 1 ones. Finally, the FC and HD components are higher in type 1 sources, with the latter showing up only in one source (with a quite spread solution around its value, see Section 4.2.3 for more details). The results presented

here suggest that LLAMA type 1 and type 2 AGN essentially host stars with the same ages, with type 1 sources showing a small bias to younger values.

#### 4.2.5 Stellar masses comparison

One of the derived quantities when fitting the stellar populations using STARLIGHT is the stellar mass. The values we derived when fitting the NIR (optical) stellar populations are listed in Table 3 (and in Table 4 for optical).

In Fig. 8 we compare the masses derived by Davies et al. (2015) using the  $H$ -band luminosity,  $L_H$ ,<sup>7</sup> with those obtained with the SP fits (top panels). We also compare in the bottom histograms of Fig. 8 the masses we obtained with those obtained by Burtcher et al. (2015, B21) for the Sy 2 of our sample and our fits using the X-shooter data (SP-OPT) with our NIR fits (SP-NIR) and those derived by Davies et al. (2015, D15) for the entire galaxy.

The median mass derived for our sample using STARLIGHT fits of the NIR spectral range is  $\log(M_*/M_\odot) = 9.04$  and for the optical  $\log(M_*/M_\odot) = 8.7$ . The median mass we have previously inferred from the optical (Burtcher et al. 2021) is  $\log(M_*/M_\odot) = 8.8$  and the median total mass of the galaxy inferred from the  $H$ -band luminosity (Davies et al. 2015) is  $\log(M_*/M_\odot) = 10.35$ . These values are roughly consistent with the fact that our apertures<sup>8</sup> cover 10–15 per cent of the

<sup>7</sup>Obtained using the equation  $\log(M_*/M_\odot) = \log(L_H/L_\odot) - 0.06$ , which has been derived comparing multiband photometry, to the integrated  $H$ -band luminosity of the galaxies studied in Koss et al. (2011).

<sup>8</sup>The aperture of the NIR data (see Table 1) is in median 70 percent of the aperture of the X-shooter data (1.8 arcsec  $\times$  1.8 arcsec).

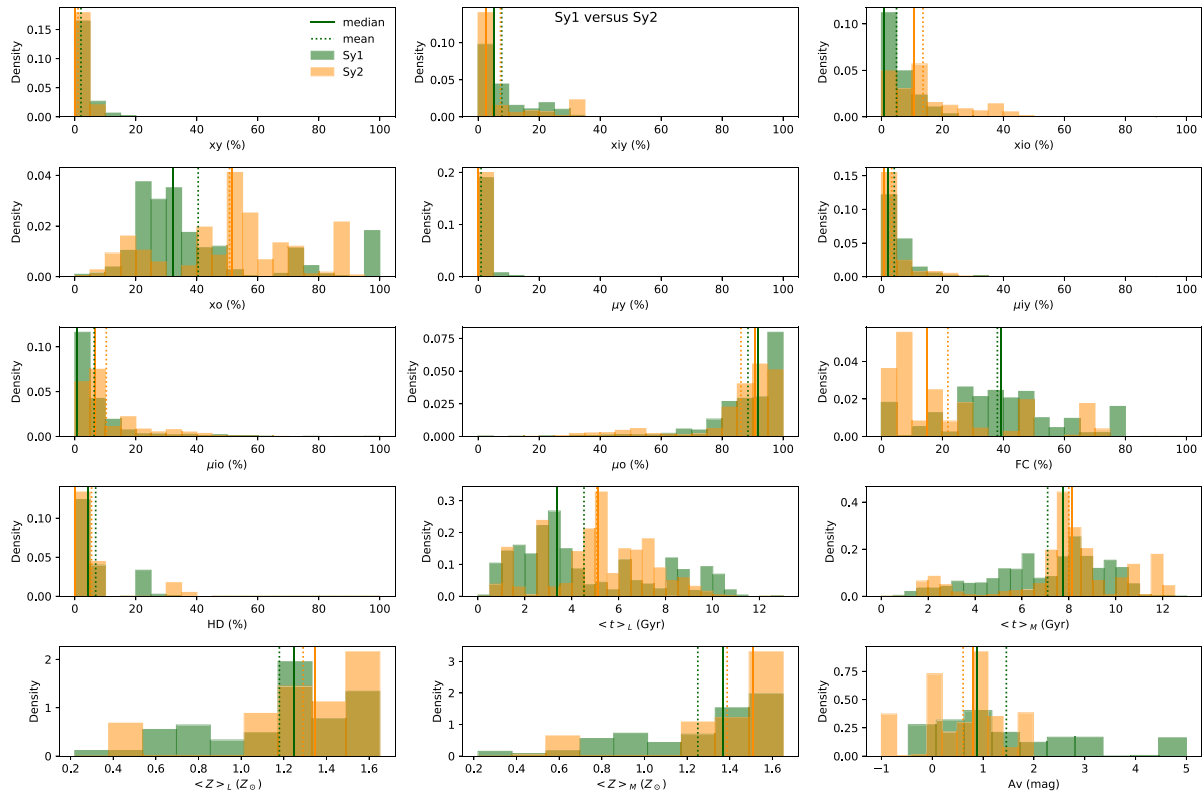


**Figure 7.** Mean stellar population properties of the Sy 1 (green) and Sy 2 (yellow) sources obtained after fitting the NIR spectral region of the 100 simulated spectra (see Section 3.1). The mean (dotted line) and the median (full line) values are shown.

mass of bulge of the LLAMA sample (see Burtscher et al. 2021, for a discussion) which has a median bulge/total ratio of 0.25 (Lin et al. 2018). It is worth mentioning that the values we have derived with the NIR data are on average two times larger than those obtained with optical data (16 times lower than those derived using  $L_H$ , while when using the optical range the values are 35 times lower than those using the  $L_H$ ). We attribute this to the fact that the NIR is more sensitive to the less luminous redder population, thus reflecting better the  $L_H$  galaxy mass estimates.

## 5 DISCUSSION

### 5.1 Comparison between the stellar population and host galaxy properties

Molecular gas serves as the essential fuel for the birth of stars. Understanding the SFH and SFR linked to each unit mass of molecular gas offers critical insights into both: the physical characteristics of the molecular phase and the surrounding conditions of star-forming regions within it.

To facilitate a comprehensive comparison of stellar population properties with the broader characteristics of host galaxies, we conducted measurements of emission line fluxes of the [O III]  $\lambda 5007$  Å and of the warm H<sub>2</sub> line  $\lambda 2.1213$   $\mu\text{m}$  on the pure emission line spectrum.<sup>9</sup> To do this we have employed the IFSCUBE code (Ruschel-Dutra et al. 2021) fitting one single Gaussian to each line.

Additionally, following the methodology presented in Riffel et al. (2021b, 2023b) we have computed the star formation rate over the

last 100 Myr for our sources using the stellar population fits. We also collected the CO luminosities,  $L'_{\text{CO}}$ , from Rosario et al. (2016) for all the LLAMA galaxies (AGN and controls). The comparison of these quantities with the stellar population properties is shown in Fig. 9.

When comparing the AGN and controls distribution, it becomes clear that in terms of [O III] both samples show different distributions, but this is expected as discussed in Rembold et al. [2017, see also Riffel et al. (2023b) and references therein]. When comparing the [O III] luminosity with  $\langle t \rangle_L$  there and  $\langle Z \rangle_L$  no correlations are seen for AGN and controls. However, AGN tend to show lower ages and metallicities when compared with their controls.

The hot molecular H<sub>2</sub> is not correlated with  $\langle t \rangle_L$ . This may indicate that in AGN the excitation of the molecular gas is mostly due to AGN. In fact, this is in agreement with the fact that H<sub>2</sub> emission is mostly due to thermal excitation mechanisms associated with the AGN (e.g. Reunanen, Kotilainen & Prieto 2002, 2003; Rodríguez-Ardila et al. 2004; Rodríguez-Ardila, Contini & Viegas 2005; Riffel et al. 2013a, 2021a, b; Colina et al. 2015; Motter et al. 2021; Bianchin et al. 2022; Holden et al. 2023).

$L'_{\text{CO}}$  shows an increasing trend with  $\langle t \rangle_L$ , however, there is no significant difference relative to the control ones. We also found that the H<sub>2</sub> luminosities are well correlated with  $L'_{\text{CO}}$ , with no clear separation between AGN and controls. In general, our results show that AGN hosts tend to have higher SFR over the last 100 Myr than the control sources.

When considering the total returned mass, a difference in the amount of returned mass over the galaxy's lifetime is seen in AGN when compared with the parent control sample. However, it is worth mentioning that taking the  $M_{\star}^{\text{Ret}}$  by populations younger than 2 Gyr ( $M_{\star}^{\text{Ret}(2\text{Gyr})}$ ) and taking the ratio over the total returned mass

<sup>9</sup>With the underlying stellar population contamination subtracted.

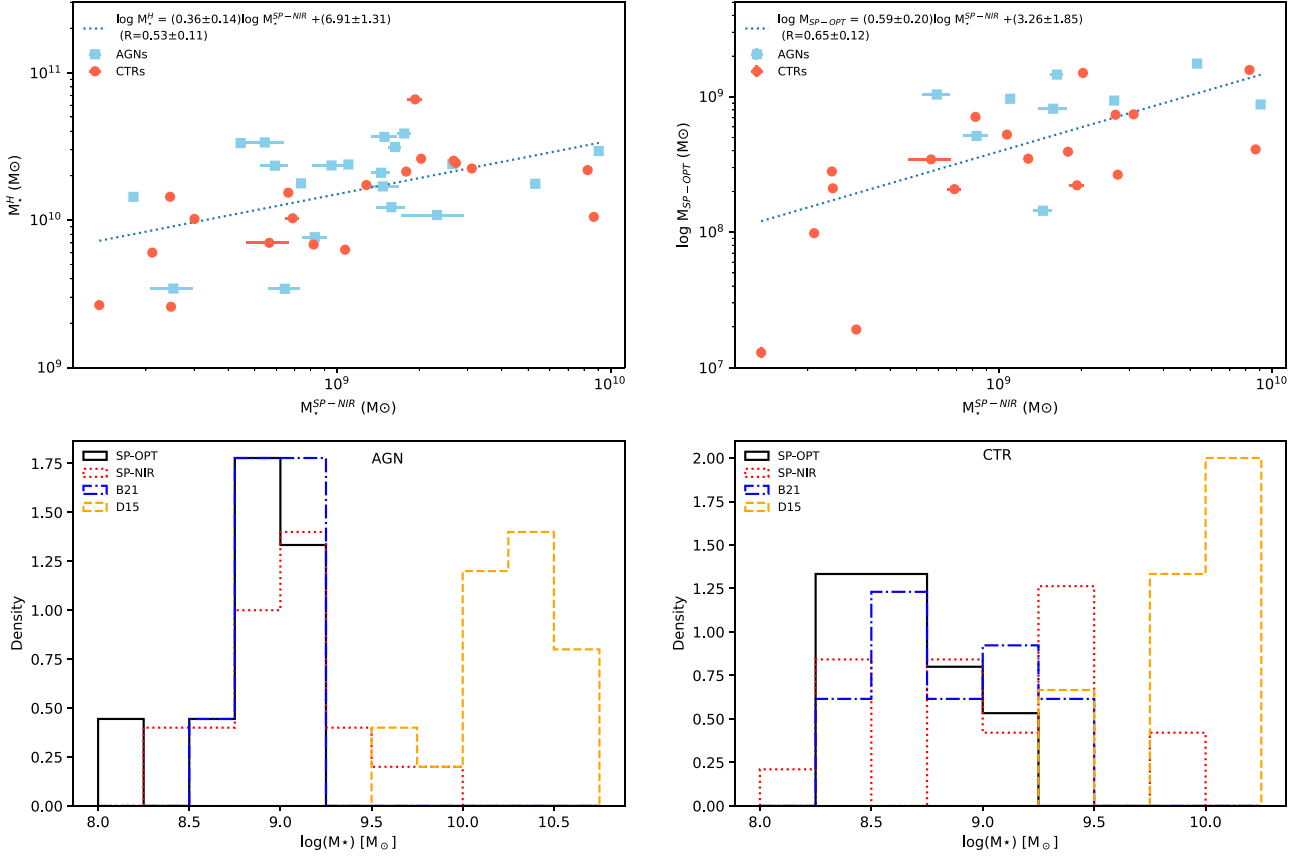


**Figure 8.** Stellar masses comparisons. The dotted line on the top panels is a linear regression over all data points using a bootstrap scheme of 1000 realizations. In the bottom panels, the different samples are labelled as follows: SP-OPT (black) our fits using the x-shooter data from Burtcher et al. (2021, with B21 (blue) being the fits obtained by these authors). SP-NIR (red) are our fits in the NIR and D15 (orange) are the masses estimated by Davies et al. (2015) for the entire galaxy.

$(M_{\star}^{\text{Ret}(2\text{Gyr})}/M_{\star}^{\text{Ret}})$  AGN do show a higher fraction than the control galaxies. The mean value for AGN (0.07) is  $\sim 2.3$  higher than the value found for the controls (0.03; see Fig. 9). Additionally, when dividing by  $M_{\star}$ , AGN show smaller values for this ratio than the controls. This means that AGN have essentially the same  $M_{\star}$  as the controls, but since they are still forming stars, they are still building their mass up, and thus this indicates that AGN are currently receiving an extra amount of gas.

To assess whether the material released by stars is sufficient to fuel the AGN, we conducted a straightforward analysis by calculating the mass accretion rate,  $\dot{M}$ , needed to generate the AGN luminosity. This calculation is expressed as follows:

$$\dot{M} = \frac{L_{\text{bol}}}{\eta c^2} \quad (7)$$

The bolometric luminosity,  $L_{\text{bol}}$ , was determined based on the methodology outlined in Ichikawa et al. (2017), given by the equation:

$$\log L_{\text{bol}} = 0.0378(\log L_{X:2-10})^2 - 2.00 \log L_{X:2-10} + 60.5, \quad (8)$$

where the intrinsic hard X-ray luminosity from Table 2 was employed. Adopting an efficiency value of  $\eta = 0.1$  (e.g. Laor & Netzer 1989; King 2008), we determined  $\dot{M}$  for our galaxy sample.

Upon comparing  $\dot{M}$  with the stellar mass returned (in  $M_{\odot} \text{ yr}^{-1}$ ), we observed that, on average, the returned mass from the intermediate population ( $M_{\star}^{\text{Ret}(2\text{Gyr})}/2\text{Gyr}$ ) is of the same order as the mass required

to sustain AGN luminosity. Note however that this is the lower limit of mass that is being released since the older population ( $t > 2 \text{ Gyr}$ ) is also present in the galaxies and is also releasing mass during these last two Gyr.<sup>10</sup> When considering the mean returned mass per year over the entire galaxy lifetime ( $M_{\star}^{\text{Ret}}/13 \text{ Gyr}$ ), the returned mass is approximately six times the mass necessary to maintain the AGN. It is noteworthy that if this analysis were conducted using  $L_X$  instead of bolometric luminosity, the resulting ratios would be approximately 20 and 120 for the mass returned over the last 2 Gyr and the galaxy's entire lifetime, respectively.

This simple exercise clarifies that there is sufficient recycled material being released by the stars in the central region (inner 100–200 pc) of the galaxies to sustain AGN luminosities (e.g. there is no need for extra gas to feed the AGN).

## 5.2 Stellar ages and AGN properties

We have also explored the impact/regulation that the energy injected by the AGN in the host galaxy may have on the star formation of our sources. Therefore we have collected several properties from literature such as  $L_X^{\text{obs}}$ ,  $L_X^{\text{int}}$ ,  $N_H$  which are only available for the AGN sample (listed Table 2). We have computed the Eddington luminosity

<sup>10</sup>It is not just the intermediate age population that is releasing mass, but the older populations are also releasing mass during this time

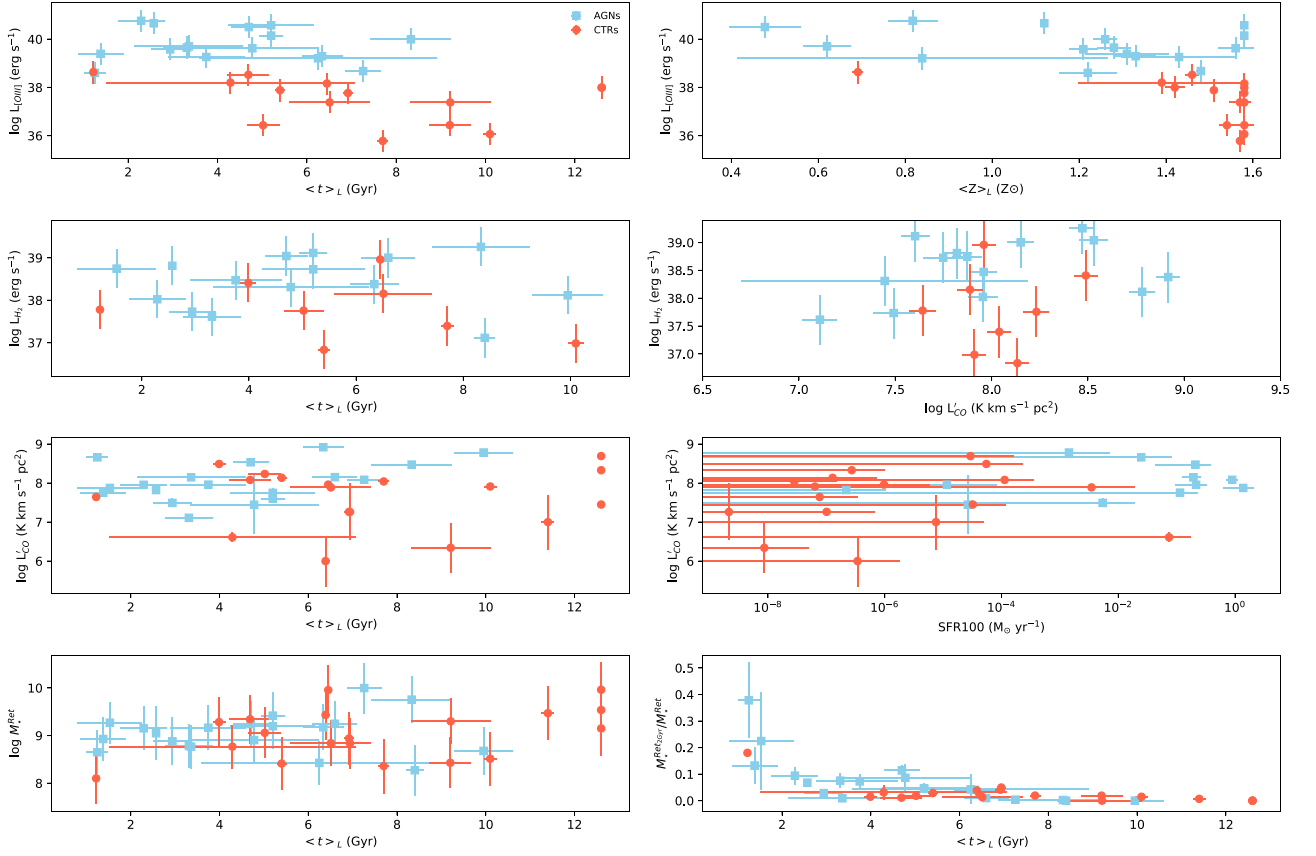


**Figure 9.** Comparisons of stellar population properties with the host galaxy properties.

using the SMBH,  $M_\bullet$ , masses listed in Table 2 and the following equation (Rybicki & Lightman 1979):

$$L_{\text{Edd}} = 1.26 \times 10^{46} \text{ erg s}^{-1} \frac{M_\bullet}{10^8 M_\odot}. \quad (9)$$

Also, following Riffel et al. (2022) the Eddington ratio was obtained from  $L_{\text{Bol}}$  [see equation (8)] and calculated using the observed and intrinsic hard X-ray luminosities ( $\lambda_{\text{obs}} = L_{\text{Bol}}^{\text{obs}}/L_{\text{Edd}}$  and  $\lambda_{\text{int}} = L_{\text{Bol}}^{\text{int}}/L_{\text{Edd}}$ ).

We have compared these properties with  $\langle t \rangle_L$ . No clear correlation is seen between these properties and the host galaxy's mean age for the stellar population, as shown by their Pearson rank correlation coefficients ( $R$  and  $p$ ):  $\log N_H$  ( $R = -0.30$ ,  $p = 0.19$ ),  $\log L_X^{\text{obs}}$  ( $R = -0.29$ ,  $p = 0.21$ ),  $\log L_X^{\text{int}}$  ( $R = -0.20$ ,  $p = 0.40$ ),  $\log \lambda_{\text{obs}}$  ( $R = -0.29$ ,  $p = 0.22$ ), and  $\log \lambda_{\text{int}}$  ( $R = -0.21$ ,  $p = 0.37$ ).

In Riffel et al. (2022) we have found that there is a positive correlation between the bolometric luminosity of the AGN with  $\langle t \rangle_M$ , however, if we consider only the LLAMA sample, no correlation is found ( $R = -0.44$ ,  $p = 0.0542$ ), but when including the lower luminosity Gemini NIFS survey sources (AGNIFS survey Riffel et al. 2017, 2022) fitted with the XSL models as described in Section 3, a positive correlation is observed (for LLAMA + AGNIFS we found  $R = 0.37$ ,  $p = 0.0234$ ). Thus, our results reinforce the conclusion that there is a delay between the formation of new stars and the triggering/feeding of the AGN.

### 5.3 Metallicities

We find that the mean stellar metallicity of the AGN hosts is lower than those of the controls. This result is in agreement with the finding

of Riffel et al. (2023b) who found that for regions  $R < 0.5 R_e$  the AGN hosts metallicity has lower values when compared with their control galaxies and larger radii values.

These results are additionally in agreement with those derived using the nebular emission. do Nascimento et al. (2022) derived the oxygen abundances in Seyfert galaxies from MaNGA, and found that the inner regions of these galaxies display lower abundances than their outer regions. Armah et al. (2023), for instance, studying the BASS sample (Koss et al. 2022; Oh et al. 2022) have shown that the more luminous Seyfert galaxies have lower gas metallicities. Our stellar metallicity estimates are qualitatively in agreement with those obtained through the gas phase abundances.<sup>11</sup> However, it is not a direct comparison as the gas metallicity represents the recent chemical evolution of galaxies, since it depends on the ionizing source (and on the production and release of oxygen to the galaxy ISM), whereas the mean stellar metallicity is an average over the entire lifespan of galaxies, including all generations of stars. Thus, stellar and nebular metallicities indeed indicate distinct evolutionary phases and respond differently to various processes that govern the chemical evolution of galaxies (Asari et al. 2007). It is worth mentioning that the stellar and gas metallicities are derived using radically different methods that they should not be compared in quantitative terms (Cid Fernandes et al. 2007). There is a huge scatter on such a comparison, but the metallicities estimated using the stellar

<sup>11</sup>In the sense that the stellar metallicities are lower in AGN than in controls and that in the gas phase oxygen abundances are lower in the AGN dominated regions when compared with the SF dominated regions.



population fitting tend to be higher when compared with the nebular one [see fig. 5(e) of Asari et al. 2007].

#### 5.4 AGN feedback energy considerations

The AGN's accretion energy release can be approximated using its hard X-ray luminosities to infer its bolometric luminosity. Here the bolometric luminosity was calculated using the intrinsic X-ray luminosity together with equation (8).

During the typical accretion phase duration when the power emanating from the central engine remains relatively constant ( $t_{\text{AGN}}$ ), a portion of the emitted energy will interact with the molecular gas. However, this interaction (termed radiation coupling:  $\epsilon_r$ ) is very uncertain (e.g. Harrison et al. 2018), but theoretical models of AGN feedback propose a value of  $\sim 5$  per cent (e.g. Di Matteo et al. 2005). From the above, we can roughly estimate the accretion power that could influence the molecular gas as  $E_{\text{Rad}} \approx \epsilon_r L_{\text{bol}} t_{\text{AGN}}$  (see Rosario et al. 2018, for details) and thus affect the star-formation in the AGN hosts. Here we adopted  $\epsilon_r = 0.05$  (Di Matteo et al. 2005) and  $t_{\text{AGN}} = 1$  Myr (Hickox et al. 2014; Schawinski et al. 2015).

According to Rosario et al. (2018) the coupling mechanism can take several forms, including direct radiation absorption by molecular or atomic clouds, or the influence of a mechanical agent like a thermal wind or relativistic particles within a jet. Assuming that  $E_{\text{Rad}}$  is distributed across all the molecular gas within the central region of AGN hosts, then its effect on the molecular gas by comparing it to the gravitational potential energy experienced by this gas, and so, this can give us some insight if the feedback might have enough power to affect the stability of this gas parcel.

Since the areas we are probing are small and in the central region of the galaxies (see Table 1) the dominant factor governing gravitational potential is the baryonic matter, encompassing both stars and gas. However, the molecular gas fraction ( $f_{\text{gas}}$ ) in the LLAMA galaxies is small and corrections for H I mass are small for disc galaxies (see Bigiel et al. 2008; Rosario et al. 2018, for details), we can assume that the potential energy experienced by this molecular gas is dominated by the stellar mass within this region (e.g. the values we have derived for it inside the extracted area of each spectrum) and its modulus can be approximated as:

$$E_{\text{PG}} \approx G \frac{M_{\star} M_{\text{H}_2}}{\eta R} (1 + f_{\text{gas}}), \quad (10)$$

where  $R$  is the radius of a circular region that will enclose the same area as the area extracted for each spectrum<sup>12</sup> and  $f_{\text{gas}} = \frac{M_{\text{H}_2}}{(M_{\text{H}_2} + M_{\star})}$  with  $M_{\text{H}_2} = \alpha_{\text{CO}} \times L'_{\text{CO}}$ . We have followed Rosario et al. (2018) and adopted  $\alpha_{\text{CO}} = 1.1 M_{\odot} \text{pc}^{-2} / (\text{K km s}^{-2})$  which is the most adequate value for metal-rich nearby galaxies (Sandstrom et al. 2013). We assumed  $\eta = 1$ , which means that the gas is uniformly distributed in a disc of size  $R$  within a uniform gravitational potential. Finally, we have corrected the  $L'_{\text{CO}}$  for aperture size<sup>13</sup> using the half-power beamwidths quoted by Rosario et al. (2018) as the radius of the CO observations. Finally, for  $M_{\star}$  we have used the values quoted in Table 3.

Taking the above assumptions as our baseline, since  $\log(E_{\text{Rad}}/E_{\text{PG}}) > 0$  for all the sources (in fact, it ranges from 1.5 to 4.5 dex; Fig. 10) it means that the energy injected by the AGN is enough to dynamically disturb the molecular gas within our aperture. The  $E_{\text{Rad}}/E_{\text{PG}}$  ratio is compared with the AGN hosts  $\langle t \rangle_L$  (top panel) and  $\langle t \rangle_M$  (bottom

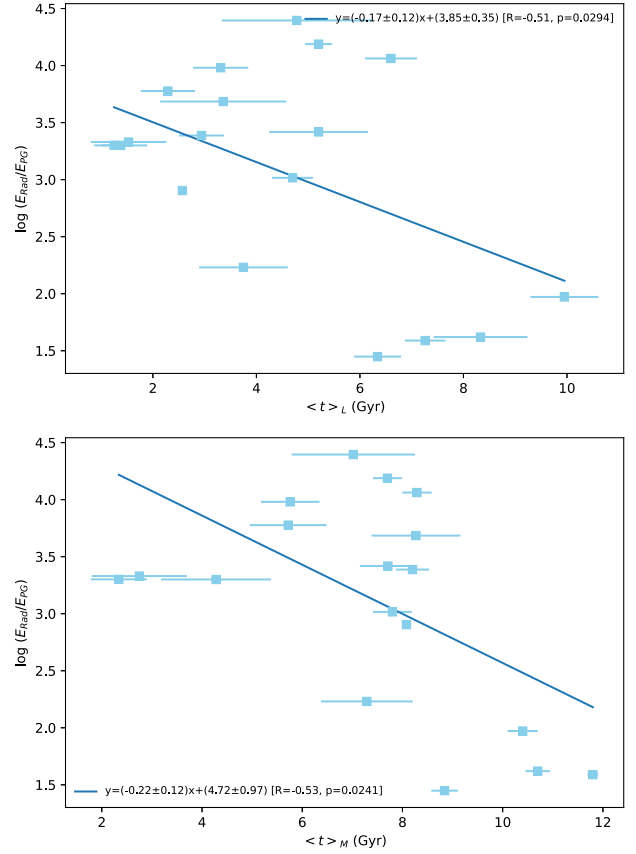


**Figure 10.** Comparison of the AGN power with the  $\langle t \rangle_L$  (top) and  $\langle t \rangle_M$  (bottom).

panel) in Fig. 10, where an anticorrelation is observed with the stellar population mean age ages (with Pearson coefficients  $R = -0.51$  and  $p = 0.0294$  for  $\langle t \rangle_L$  and  $R = -0.53$  and  $p = 0.0241$  for  $\langle t \rangle_M$ ). This can be interpreted as the fact that the AGN is affecting the star formation in these galaxies, in the sense that more energetic AGN [ $\log(E_{\text{Rad}}/E_{\text{PG}}) \gtrsim 3$ ] tend to host younger nuclear stellar populations  $\langle t \rangle_L \lesssim 4 \text{ Gyr}$  ( $\langle t \rangle_M \lesssim 7 \text{ Gyr}$ ) or that these galaxies do have a more extended SF history since the LLAMA AGN do not have a larger amount of molecular gas when compared with their controls (Rosario et al. 2018).

It is worth mentioning that the trend observed here might be a caveat of the correction for aperture of the  $L'_{\text{CO}}$ , which assumes a uniform distribution of the molecular gas within the APEX beam collecting area. For instance, high-resolution ALMA observations of a volume-limited sample of X-ray selected AGN part of the galactic activity, torus, and outflow survey (GATOS) revealed the imprint of AGN feedback in the central gas concentration of Seyfert galaxies. The GATOS AGN with higher luminosity show more outflows and more molecular gas deficits, supporting a scenario in which AGN winds are more likely to push away the gas in the centre as the AGN luminosity increases (García-Burillo et al. 2021). The same is also observed in hot molecular gas ( $\text{H}_2$ ; Riffel et al. 2023a). To confirm the results obtained for the LLAMA AGN sample, we need resolved observation of the cold gas with ALMA.

#### 5.5 The role played by the recycled material in AGN fuelling

Basically to trigger or sustain an AGN what is required is that enough fuel reaches the accretion disc. Such fuel (e.g. gas) can have

<sup>12</sup>  $R = \sqrt{(\text{slit width} \times \text{aperture})/\pi}$ .

<sup>13</sup>  $L'_{\text{CO}}$  corrected =  $L'_{\text{CO}}$  (Area NIR aperture/Area Radio Aperture).

an external origin, coming from mergers or tidal interactions (e.g. Araujo et al. 2023; Raimundo, Malkan & Vestergaard 2023; Rembold et al. 2024, and references therein). In the case of the LLAMA AGN, Davies et al. (2017) has studied the environment of these sources. They mostly are in small or large groups, so external gas could be stripped out of other galaxies or minor mergers could play some role. However, this gas will unlikely directly feed the AGN, since it would have to reach the inner region of the galaxy. Such gas could perturb the gas already in the galaxy [LLAMA galaxies are mostly spirals, see Table 1, thus having enough recycled + pristine gas to keep SF and AGN activity (Vazdekis et al. 1996)], making it reach the central region more efficiently, however, while it moves inwards it would also form stars. Finally, Davies et al. (2017) concluded that the LLAMA AGN do not show evidence of environmental dependence.

The observational results presented here show that AGN do have a larger fraction of intermediate-age stellar populations when compared with their matched analogues. Such an intermediate age population is dominated by massive ( $M \simeq 1.5 - 10 M_{\odot}$ ;  $200 \text{ Myr} \lesssim t \lesssim 2 \text{ Gyr}$ ) evolved stars (e.g. Dottori et al. 2005; Maraston 2005; Riffel et al. 2007, 2008b, 2015, 2022, 2023b; Salaris et al. 2014; Dahmer-Hahn et al. 2022, in the RGB and TP-AGB phases), that do release a high amount of enriched material to the nuclear environment.

Very recently Choi et al. (2023) have used the suite of cosmological hydrodynamical simulations of massive galaxies and supermassive black hole formation presented in Choi et al. (2017) to investigate the origins of the gas-accreted by the SMBH. They have found that recycled gas generated within the host galaxies, e.g. ejected from evolved stars (SN and AGB stars) contributes, on average, with  $\sim 40$  per cent of the fuel for AGN. This gas also contributes to the formation of new stars but in a lower fraction ( $\sim 20$  per cent), being the external gas the major source of fuel for the formation of new stars. In their simulations, *in-situ* star formation has a higher contribution from pristine and cosmic web accretion compared to black hole feeding.

Nevertheless, they argue that this does not imply that a higher proportion of the overall recycled gas released by evolved stars contributes directly to the feeding of the black holes. In reality, given that the total gas used in star formation far exceeds the gas accreted by black holes, the sheer volume of recycled gas consumed by star formation greatly surpasses the quantity acquired by black holes. However, they show that the relatively higher proportion of recycled gas within the black hole mass budget, as compared to that attributed to star formation, suggests that recycled gas is notably efficient in feeding the SMBH, surpassing the other sources of gas entering the host galaxy. This is because this high metallicity gas cools down very efficiently and because it is abundantly released very close to the centre of the galaxy. Finally the lower (but still high,  $\langle Z \rangle_L > 0.4 Z_{\odot}$ ) stellar metallicity found in the AGN when compared with the control galaxies can be attributed to the fact that spiral galaxies do have a high amount of gas that has never been converted into stars (Vazdekis et al. 1996). This is associated with the fact that molecular gas is very turbulent in more luminous AGN (García-Burillo et al. 2021), thus making the mix of the low and high metallicity gas more efficient in AGN than in the control galaxies. Therefore diluting the overall gas phase metallicity in AGN.

The gas released by the intermediate age stars has a low velocity (a few hundred  $\text{km s}^{-1}$ ) and is accreted together with the gas already available in the central region (e.g. Cuadra et al. 2006; Davies et al. 2007; Riffel et al. 2022, 2023b). It has been demonstrated in previous works that this extra amount of gas will trigger the AGN or make it more powerful and/or form new stars (e.g. Ciotti & Ostriker 2007; Ciotti, Ostriker & Proga 2010; Leitner & Kravtsov 2011; Segers et al.

2016; Salvador-Rusiñol et al. 2020, 2021; Benedetti et al. 2023; Riffel et al. 2023a, and references therein).

The larger fractions of stellar material released by the AGN when compared with the controls agree with the results found in the simulations, in the sense that besides being more abundant on AGN than in the controls, this gas is released very close to the AGN and the stars provide an efficient angular momentum sink making the gas falling more efficiently towards the SMBH (Hopkins 2012). In this way, this recycled material acts as a ‘seasoning,’ making the supermassive black hole ‘food’ more flavourful.

## 6 CONCLUSIONS

We have used near-infrared spectroscopy to study the stellar population of the complete LLAMA sample (20 AGNs) and compared them with their matched analogues (19 inactive galaxies). Therefore we have employed the new XSL models together with the STARLIGHT code. Our main conclusions can be summarized as follows:

- (i) The star formation history of the sources is very complex, presenting many episodes of star formation during their lifetimes.
- (ii) Optical and NIR properties derived for type 2 AGNs and controls are in very good agreement. For the NIR we have also fitted the type 1 sources and provided their stellar properties.
- (iii) AGN hosts have higher fractions of intermediate-age, less metallic stellar populations when compared with the control sample. The AGNs are more affected by reddening and, as expected, only they require significant fractions of FC and HD components to fit their underlying continuum. We have obtained mean/median values of the  $\langle t \rangle_L$  (4.7/4.5 Gyr for AGNs and 7.5/6.9 Gyr for the controls) as well as in the mean/median values for  $\langle t \rangle_M$  (7.5/8.0 Gyr for AGNs and 10.2/10.2 Gyr for the controls).
- (iv) No correlations between host galaxy gas properties (e.g. CO luminosity, hot  $\text{H}_2$  luminosity, [O III] luminosity) have been observed with age.
- (v) The  $E_{\text{Rad}}/E_{\text{PG}}$  ratio for AGN is compared with the  $\langle t \rangle_L$  and an anticorrelation is observed with the stellar population mean age (with Pearson coefficients  $R = -0.48$  and  $p = 0.043$ ). This suggests that the AGN is affecting the star formation in these galaxies, in the sense that more energetic AGNs ( $\log(E_{\text{Rad}}/E_{\text{PG}}) \gtrsim 3$ ) tend to host younger nuclear stellar populations  $\langle t \rangle_L \lesssim 4 \text{ Gyr}$  ( $\langle t \rangle_M \lesssim 7 \text{ Gyr}$ ).
- (vi) The role played by the stellar recycled material in AGN fuelling is discussed. We found that the recent ( $t < 2 \text{ Gyr}$ ) returned (recycled) stellar mass is higher in AGN than in the controls. We discuss and provide evidence to models that support that AGN feeding is, at least, partially driven by the recycled material originating from stellar evolution.

In general, our results point towards the fact that the central region of AGN are dominated by young to intermediate-age stellar populations when compared with their control galaxies. We also provide evidence that the mass-loss of stars would be enough to feed the AGNs, thus providing observational constraints for models that predict that AGN feeding is primarily due to the recycled gas from dying stars.

## ACKNOWLEDGEMENTS

We thank the anonymous referee for useful suggestions that helped improve the paper. We thank Ena Choi, Roberto Cid Fernandes, and Natalia Vale Asari for the useful discussion. RR acknowledges support from the Fundación Jesús Serra and the Instituto de Astrofísica de Canarias under the Visiting Researcher Programme 2023–2025

agreed between both institutions. RR, also acknowledges support from the ACIISI, Consejería de Economía, Conocimiento y Empleo del Gobierno de Canarias and the European Regional Development Fund (ERDF) under grant with reference ProID2021010079, and the support through the RAVET project by the grant PID2019-107427GB-C32 from the Spanish Ministry of Science, Innovation and Universities MCIU. This work has also been supported through the IAC project TRACES, which is partially supported through the state budget and the regional budget of the Consejería de Economía, Industria, Comercio y Conocimiento of the Canary Islands Autonomous Community. RR also thanks to Conselho Nacional de Desenvolvimento Científico e Tecnológico (CNPq, Proj. 311223/2020-6, 304927/2017-1 and 400352/2016-8), Fundação de amparo à pesquisa do Rio Grande do Sul (FAPERGS, Proj. 16/2551-0000251-7 and 19/1750-2), Coordenação de Aperfeiçoamento de Pessoal de Nível Superior (CAPES, Proj. 0001). LGDH acknowledges support by National Key R&D Program of China No.2022YFF0503402. LM thanks FAPESP (grant 2022/03703-1) and CNPq (grant 306359/2018-9) for partial funding of this research. RAR thanks financial support from FAPERGS (21/2551-0002018-0), CNPq (303450/2022-3, 403398/2023-1, 441722/2023-7) and CAPES (88887.894973/2023-00). ARA acknowledges Conselho Nacional de Desenvolvimento Científico e Tecnológico (CNPq) for partial support to this work through grant 312036/2019-1. MT thanks the support from CNPq (process 312541/2021-0). CRA and AA acknowledge funding from the State Research Agency (AEI-MCINN) of the Spanish Ministry of Science and Innovation under the grant ‘Tracking active galactic nuclei feedback from parsec to kiloparsec scales’, with reference PID2022-141105NB-I00.

## DATA AVAILABILITY

The data will be made available under reasonable request.

## REFERENCES

- Ajello M., Alexander D. M., Greiner J., Madejski G. M., Gehrels N., Burlon D., 2012, *ApJ*, 749, 21
- Araujo B. L. C., Storchi-Bergmann T., Rembold S. B., Kaipper A. L. P., Dall’Agnol de Oliveira B., 2023, *MNRAS*, 522, 5165
- Armah M. et al., 2023, *MNRAS*, 520, 1687
- Asari N. V., Cid Fernandes R., Stasińska G., Torres-Papaqui J. P., Mateus A., Sodré L., Schoenell W., Gomes J. M., 2007, *MNRAS*, 381, 263
- Audibert A. et al., 2019, *A&A*, 632, A33
- Audibert A. et al., 2021, *A&A*, 656, A60
- Barvainis R., 1987, *ApJ*, 320, 537
- Benedetti J. P. V. et al., 2023, *MNRAS*, 522, 2570
- Bertolami M. M. M., 2016, *A&A*, 588, A25
- Bessiere P. S., Ramos Almeida C., 2022, *MNRAS*, 512, L54
- Bessiere P. S., Tadhunter C. N., Ramos Almeida C., Villar Martín M., Cabrera-Lavers A., 2017, *MNRAS*, 466, 3887
- Bianchin M. et al., 2022, *MNRAS*, 510, 639
- Bica E., Alloin D., 1987, *A&A*, 186, 49
- Bieri R., Dubois Y., Silk J., Mamon G. A., Gaibler V., 2016, *MNRAS*, 455, 4166
- Bigiel F., Leroy A., Walter F., Brinks E., de Blok W. J. G., Madore B., Thornley M. D., 2008, *AJ*, 136, 2846
- Bruzual G., Charlot S., 2003, *MNRAS*, 344, 1000
- Burtscher L. et al., 2015, *A&A*, 578, A47
- Burtscher L. et al., 2021, *A&A*, 654, A132
- Caglar T. et al., 2020, *A&A*, 634, A114
- Cappellari M., 2017, *MNRAS*, 466, 798
- Cardelli J. A., Clayton G. C., Mathis J. S., 1989, *ApJ*, 345, 245
- Chen Y., Bressan A., Girardi L., Marigo P., Kong X., Lanza A., 2015, *MNRAS*, 452, 1068
- Choi E., Ostriker J. P., Naab T., Somerville R. S., Hirschmann M., Núñez A., Hu C.-Y., Oser L., 2017, *ApJ*, 844, 31
- Choi E., Somerville R. S., Ostriker J. P., Hirschmann M., Naab T., 2023, *The Origins of Gas Accreted by Supermassive Black Holes: The Importance of Recycled Gas*.
- Cid Fernandes R., 2018, *MNRAS*, 480, 4480
- Cid Fernandes R., Jr, Terlevich R., 1995, *MNRAS*, 272, 423
- Cid Fernandes R., Gu Q., Melnick J., Terlevich E., Terlevich R., Kunth D., Rodrigues Lacerda R., Joguet B., 2004, *MNRAS*, 355, 273
- Cid Fernandes R., Mateus A., Sodré L., Stasińska G., Gomes J. M., 2005, *MNRAS*, 358, 363
- Cid Fernandes R., Asari N. V., Sodré L., Stasińska G., Mateus A., Torres-Papaqui J. P., Schoenell W., 2007, *MNRAS*, 375, L16
- Cid Fernandes R. et al., 2013, *A&A*, 557, A86
- Ciotti L., Ostriker J. P., 2007, *ApJ*, 665, 1038
- Ciotti L., Ostriker J. P., Proga D., 2010, *ApJ*, 717, 708
- Colina L. et al., 2015, *A&A*, 578, A48
- Conroy C., 2013, *ARA&A*, 51, 393
- Cuadra J., Nayakshin S., Springel V., Di Matteo T., 2006, *MNRAS*, 366, 358
- Cushing M. C., Vacca W. D., Rayner J. T., 2004, *PASP*, 116, 362
- Dahmer-Hahn L. G. et al., 2022, *MNRAS*, 509, 4653
- Dametto N. Z., Riffel R., Pastoriza M. G., Rodríguez-Ardila A., Hernandez-Jimenez J. A., Carvalho E. A., 2014, *MNRAS*, 443, 1754
- Davies R. I., Sternberg A., Lehnert M. D., Tacconi-Garman L. E., 2005, *ApJ*, 633, 105
- Davies R. I., Müller Sánchez F., Genzel R., Tacconi L. J., Hicks E. K. S., Friedrich S., Sternberg A., 2007, *ApJ*, 671, 1388
- Davies R. I., Maciejewski W., Hicks E. K. S., Tacconi L. J., Genzel R., Engel H., 2009, *ApJ*, 702, 114
- Davies R. I. et al., 2015, *ApJ*, 806, 127
- Davies R. I. et al., 2017, *MNRAS*, 466, 4917
- de Lorenzo-Cáceres A., Vazdekis A., Falcón-Barroso J., Beasley M. A., 2020, *MNRAS*, 498, 1002
- De Vaucouleurs G., 1959, in Flüge S., ed., *Handbuch Der Physik/Encyclopedia of Physics, Astrophysik IV: Sternsysteme/Astrophysics IV: Stellar Systems*. Springer, Berlin, Heidelberg, p. 275,
- Di Matteo T., Springel V., Hernquist L., 2005, *Nature*, 433, 604
- Dias B., Coelho P., Barbuy B., Kerber L., Idiart T., 2010, *A&A*, 520, A85
- Diniz M. R. et al., 2017, *MNRAS*, 469, 3286
- Diniz M. R., Riffel R. A., Storchi-Bergmann T., Riffel R., 2019, *MNRAS*, 487, 3958
- do Nascimento J. C. et al., 2022, *MNRAS*, 513, 807
- Dottori H., Díaz R. J., Carranza G., Lípári S., Santos J., Jr, 2005, *ApJ*, 628, L85
- El-Badry K., Wetzel A., Geha M., Hopkins P. F., Kereš D., Chan T. K., Faucher-Giguère C.-A., 2016, *ApJ*, 820, 131
- Ellison S. L., Teimoorinia H., Rosario D. J., Mendel J. T., 2016, *MNRAS*, 458, L34
- Ellison S. L. et al., 2021, *MNRAS*, 505, L46
- Esquej P. et al., 2014, *ApJ*, 780, 86
- Fabian A. C., 2012, *ARA&A*, 50, 455
- Fathi K., Storchi-Bergmann T., Riffel R. A., Winge C., Axon D. J., Robinson A., Capetti A., Marconi A., 2006, *ApJ*, 641, L25
- Ferrarese L., Merritt D., 2000, *ApJ*, 539, L9
- Gallagher R., Maiolino R., Belfiore F., Drory N., Riffel R., Riffel R. A., 2019, *MNRAS*, 485, 3409
- García-Burillo S. et al., 2021, *A&A*, 652, A98
- Gaspar G., Díaz R. J., Mast D., D’Ambra A., Agüero M. P., Günthardt G., 2019, *AJ*, 157, 44
- Ge J., Yan R., Cappellari M., Mao S., Li H., Lu Y., 2018, *MNRAS*, 478, 2633
- Gebhardt K. et al., 2000, *ApJ*, 539, L13
- Goddard D. et al., 2017, *MNRAS*, 465, 688
- Gomes J. M., Papaderos P., 2017, *A&A*, 603, A63
- González Delgado R. M., Heckman T., Leitherer C., 2001, *ApJ*, 546, 845
- Granato G. L., Danese L., 1994, *MNRAS*, 268, 235



- Granato G. L., De Zotti G., Silva L., Bressan A., Danese L., 2004, *ApJ*, 600, 580
- Harrison C. M., Costa T., Tadhunter C. N., Flütsch A., Kakkad D., Perna M., Vietri G., 2018, *Nat. Astron.*, 2, 198
- Heckman T. M., Best P. N., 2014, *ARA&A*, 52, 589
- Hennig M. G., Riffel R. A., Dors O. L., Riffel R., Storchi-Bergmann T., Colina L., 2018, *MNRAS*, 477, 1086
- Hickox R. C., Mullaney J. R., Alexander D. M., Chen C.-T. J., Civano F. M., Goulding A. D., Hainline K. N., 2014, *ApJ*, 782, 9
- Holden L. R., Tadhunter C. N., Morganti R., Oosterloo T., 2023, *MNRAS*, 520, 1848
- Hopkins P. F., 2012, *MNRAS*, 420, L8
- Hopkins P. F., Hernquist L., 2010, *MNRAS*, 407, 447
- Ichikawa K., Ricci C., Ueda Y., Matsuoka K., Toba Y., Kawamuro T., Trakhtenbrot B., Koss M. J., 2017, *ApJ*, 835, 74
- Imanishi M., Wada K., 2004, *ApJ*, 617, 214
- Ishibashi W., Fabian A. C., 2012, *MNRAS*, 427, 2998
- Jarrett T. H., Chester T., Cutri R., Schneider S. E., Huchra J. P., 2003, *AJ*, 125, 525
- Johnson B. D., Leja J., Conroy C., Speagle J. S., 2021, *ApJS*, 254, 22
- King A., 2008, *New Astron. Rev.*, 52, 253
- King A., Pounds K., 2015, *ARA&A*, 53, 115
- Koleva M., Prugniel Ph., Ocvirk P., Le Borgne D., Soubiran C., 2008, *MNRAS*, 385, 1998
- Koleva M., Prugniel P., Bouchard A., Wu Y., 2009, *A&A*, 501, 1269
- Koski A. T., 1978, *ApJ*, 223, 56
- Koss M., Mushotzky R., Veilleux S., Winter L. M., Baumgartner W., Tueller J., Gehrels N., Valencic L., 2011, *ApJ*, 739, 57
- Koss M. J. et al., 2022, *ApJS*, 261, 2
- Kroupa P., 2001, *MNRAS*, 322, 231
- LaMassa S. M., Heckman T. M., Ptak A., Martins L., Wild V., Sonnentrucker P., 2010, *ApJ*, 720, 786
- Laor A., Netzer H., 1989, *MNRAS*, 238, 897
- Leitner S. N., Kravtsov A. V., 2011, *ApJ*, 734, 48
- Lin M.-Y. et al., 2018, *MNRAS*, 473, 4582
- Madau P., Dickinson M., 2014, *ARA&A*, 52, 415
- Magorrian J. et al., 1998, *AJ*, 115, 2285
- Maiolino R. et al., 2017, *Nature*, 544, 202
- Mallmann N. D. et al., 2018, *MNRAS*, 478, 5491
- Maraston C., 2005, *MNRAS*, 362, 799
- Martini P., Regan M. W., Mulchaey J. S., Pogge R. W., 2003, *ApJ*, 589, 774
- Martins L. P., Riffel R., Rodríguez-Ardila A., Gruenwald R., de Souza R., 2010, *MNRAS*, 406, 2185
- Mason R. E. et al., 2015, *ApJS*, 217, 13
- Mercedes-Feliz J. et al., 2023, *MNRAS*, 524, 3446
- Motter J. C. et al., 2021, *MNRAS*, 506, 4354
- Müller Sánchez F., Davies R. I., Genzel R., Tacconi L. J., Eisenhauer F., Hicks E. K. S., Friedrich S., Sternberg A., 2009, *ApJ*, 691, 749
- Nayakshin S., Zubovas K., 2012, *MNRAS*, 427, 372
- Novak G. S., Ostriker J. P., Ciotti L., 2011, *ApJ*, 737, 26
- Ocvirk P., Pichon C., Lançon A., Thiébaud E., 2006, *MNRAS*, 365, 46
- Oh K. et al., 2022, *ApJS*, 261, 4
- Oliva E., Origlia L., Kotilainen J. K., Moorwood A. F. M., 1995, *A&A*, 301, 55
- Panther B., Jimenez R., Heavens A. F., Charlot S., 2007, *MNRAS*, 378, 1550
- Pastorelli G. et al., 2020, *MNRAS*, 498, 3283
- Raimundo S. I., Malkan M., Vestergaard M., 2023, *Nat. Astron.*, 7, 463
- Rayner J. T., Toomey D. W., Onaka P. M., Denault A. J., Stahlberger W. E., Vacca W. D., Cushing M. C., Wang S., 2003, *PASP*, 115, 362
- Rees M. J., 1989, *MNRAS*, 239, 1P
- Rembold S. B. et al., 2017, *MNRAS*, 472, 4382
- Rembold S. B. et al., 2024, *MNRAS*, 527, 6722
- Reunanen J., Kotilainen J. K., Prieto M. A., 2002, *MNRAS*, 331, 154
- Reunanen J., Kotilainen J. K., Prieto M. A., 2003, *MNRAS*, 343, 192
- Ricci C., Ueda Y., Koss M. J., Trakhtenbrot B., Bauer F. E., Gandhi P., 2015, *ApJ*, 815, L13
- Ricci C. et al., 2017, *ApJS*, 233, 17
- Riffel R., Rodríguez-Ardila A., Pastoriza M. G., 2006, *A&A*, 457, 61
- Riffel R., Pastoriza M. G., Rodríguez-Ardila A., Maraston C., 2007, *ApJ*, 659, L103
- Riffel R. A., Storchi-Bergmann T., Winge C., McGregor P. J., Beck T., Schmitt H., 2008a, *MNRAS*, 385, 1129
- Riffel R., Pastoriza M. G., Rodríguez-Ardila A., Maraston C., 2008b, *MNRAS*, 388, 803
- Riffel R., Pastoriza M. G., Rodríguez-Ardila A., Bonatto C., 2009, *MNRAS*, 400, 273
- Riffel R. A., Storchi-Bergmann T., Riffel R., Pastoriza M. G., 2010, *ApJ*, 713, 469
- Riffel R., Ruschel-Dutra D., Pastoriza M. G., Rodríguez-Ardila A., Santos J. F. C. Jr., Bonatto C. J., Ducati J. R., 2011a, *MNRAS*, 410, 2714
- Riffel R., Riffel R. A., Ferrari F., Storchi-Bergmann T., 2011b, *MNRAS*, 416, 493
- Riffel R., Rodríguez-Ardila A., Aleman I., Brotherton M. S., Pastoriza M. G., Bonatto C., Dors O. L., 2013a, *MNRAS*, 430, 2002
- Riffel R. A., Storchi-Bergmann T., Winge C., 2013b, *MNRAS*, 430, 2249
- Riffel R. et al., 2015, *MNRAS*, 450, 3069
- Riffel R. A. et al., 2016, *MNRAS*, 461, 4192
- Riffel R. A., Storchi-Bergmann T., Riffel R., Dahmer-Hahn L. G., Diniz M. R., Schönell A. J., Dametto N. Z., 2017, *MNRAS*, 470, 992
- Riffel R. et al., 2019, *MNRAS*, 486, 3228
- Riffel R. A., Bianchin M., Riffel R., Storchi-Bergmann T., Schönell A. J., Dahmer-Hahn L. G., Dametto N. Z., Diniz M. R., 2021a, *MNRAS*, 503, 5161
- Riffel R. A. et al., 2021b, *MNRAS*, 504, 3265
- Riffel R. et al., 2022, *MNRAS*, 512, 3906
- Riffel R. A. et al., 2023a, *MNRAS*, 521, 1832
- Riffel R. et al., 2023b, *MNRAS*, 524, 5640
- Rodríguez-Ardila A., Pastoriza M. G., Viegas S., Sigut T. a. A., Pradhan A. K., 2004, *A&A*, 425, 457
- Rodríguez-Ardila A., Contini M., Viegas S. M., 2005, *MNRAS*, 357, 220
- Rosario D. J., Mendel J. T., Ellison S. L., Lutz D., Trump J. R., 2016, *MNRAS*, 457, 2703
- Rosario D. J. et al., 2018, *MNRAS*, 473, 5658
- Ruschel-Dutra D., Rodríguez Espinosa J. M., González Martín O., Pastoriza M., Riffel R., 2017, *MNRAS*, 466, 3353
- Ruschel-Dutra D. et al., 2021, *MNRAS*, 507, 74
- Rybicki G. B., Lightman A. P., 1979, *Radiative Processes in Astrophysics*. Wiley-Interscience, New York, 393 p.
- Salaris M., Weiss A., Cassarà L. P., Piovani L., Chiosi C., 2014, *A&A*, 565, A9
- Sales D. A., Pastoriza M. G., Riffel R., Winge C., Rodríguez-Ardila A., Carciofi A. C., 2011, *ApJ*, 738, 109
- Sales D. A., Ruschel-Dutra D., Pastoriza M. G., Riffel R., Winge C., 2014, *MNRAS*, 441, 630
- Salvador-Rusiñol N., Vazdekis A., La Barbera F., Beasley M. A., Ferreras I., Negri A., Dalla Vecchia C., 2020, *Nat. Astron.*, 4, 252
- Salvador-Rusiñol N., Beasley M. A., Vazdekis A., Barbera F. L., 2021, *MNRAS*, 500, 3368
- Sánchez S. F. et al., 2016, *Rev. Mex. Astron. Astrofis.*, 52, 21
- Sandstrom K. M. et al., 2013, *ApJ*, 777, 5
- Schawinski K., Koss M., Berney S., Sartori L. F., 2015, *MNRAS*, 451, 2517
- Schmidt A. A., Copetti M. V. F., Alloin D., Jablonka P., 1991, *MNRAS*, 249, 766
- Segers M. C., Crain R. A., Schaye J., Bower R. G., Furlong M., Schaller M., Theuns T., 2016, *MNRAS*, 456, 1235
- Silva-Lima L. A., Martins L. P., Coelho P. R. T., Gadotti D. A., 2022, *A&A*, 661, A105
- Skrutskie M. F. et al., 2006, *AJ*, 131, 1163
- Storchi-Bergmann T., Schnorr-Müller A., 2019, *Nat. Astron.*, 3, 48
- Storchi-Bergmann T., González Delgado R. M., Schmitt H. R., Cid Fernandes R., Heckman T., 2001, *ApJ*, 559, 147
- Storchi-Bergmann T., Riffel R. A., Riffel R., Diniz M. R., Borges Vale T., McGregor P. J., 2012, *ApJ*, 755, 87
- Terlevich E., Diaz A. I., Terlevich R., 1990, *MNRAS*, 242, 271
- Terrazas B. A. et al., 2020, *MNRAS*, 493, 1888
- Tojeiro R., Heavens A. F., Jimenez R., Panther B., 2007, *MNRAS*, 381, 1252



Trussler J., Maiolino R., Maraston C., Peng Y., Thomas D., Goddard D., Lian J., 2020, *MNRAS*, 491, 5406  
 Vacca W. D., Cushing M. C., Rayner J. T., 2003, *PASP*, 115, 389  
 Vazdekis A., Casuso E., Peletier R. F., Beckman J. E., 1996, *ApJS*, 106, 307  
 Verro K. et al., 2022a, *A&A*, 660, A34  
 Verro K. et al., 2022b, *A&A*, 661, A50  
 Walcher J., Groves B., Budavári T., Dale D., 2011, *Ap&SS*, 331, 1  
 Wang X., Loeb A., 2018, *New Astron.*, 61, 95  
 Weinberger R. et al., 2023, *MNRAS*, 523, 1104  
 Wilkinson D. M., Maraston C., Goddard D., Thomas D., Parikh T., 2017, *MNRAS*, 472, 4297  
 Woo J., Walters D., Archinuk F., Faber S. M., Ellison S. L., Teimoorinia H., Iyer K., 2024, *MNRAS*,  
 Worthey G., Faber S. M., Gonzalez J. J., Burstein D., 1994, *ApJS*, 94, 687  
 Zubovas K., Bourne M. A., 2017, *MNRAS*, 468, 4956  
 Zubovas K., Nayakshin S., King A., Wilkinson M., 2013, *MNRAS*, 433, 3079

## SUPPORTING INFORMATION

Supplementary data are available at [MNRAS](https://www.mnras.org) online.

**Appendix A.** Final reduced spectra.

**Appendix B.** Individual stellar population fits.

Please note: Oxford University Press is not responsible for the content or functionality of any supporting materials supplied by the authors. Any queries (other than missing material) should be directed to the corresponding author for the article.

<sup>1</sup>*Departamento de Astronomia, Instituto de Física, Universidade Federal do Rio Grande do Sul, CP 15051, 91501-970, Porto Alegre, RS, Brazil*

<sup>2</sup>*Instituto de Astrofísica de Canarias, Calle Vía Láctea s/n, E-38205 La Laguna, Tenerife, Spain*

<sup>3</sup>*Shanghai Astronomical Observatory, Chinese Academy of Sciences, 80 Nandan Road, Shanghai 200030, China*

<sup>4</sup>*Departamento de Astrofísica, Universidad de La Laguna, E-38205 Tenerife, Spain*

<sup>5</sup>*Max-Planck-Institut für extraterrestrische Physik, Postfach 1312, D-85741 Garching, Germany*

<sup>6</sup>*Centre for Extragalactic Astronomy, Department of Physics, Durham University, South Road, Durham DH1 3LE, UK*

<sup>7</sup>*NAT – Universidade Cidade de São Paulo, Rua Galvão Bueno, 868, 01506-000, São Paulo, SP, Brazil*

<sup>8</sup>*Laboratório Nacional de Astrofísica – Rua dos Estados Unidos 154, Bairro das Nações. CEP 37504-364 Itajubá, MG, Brazil*

<sup>9</sup>*Observatório Nacional, Rua General José Cristino 77, CEP 20921-400 São Cristóvão, Rio de Janeiro, RJ, Brazil*

<sup>10</sup>*Instituto Nacional de Pesquisas Espaciais, Av. dos Astronautas, 1758 - Jardim da Granja São José dos Campos/SP - 12227-010, Brazil*

<sup>11</sup>*Departamento de Física/CCNE, Universidade Federal de Santa Maria, 97105-900 Santa Maria, RS, Brazil.*

<sup>12</sup>*Department of Physics and Astronomy, University of Alaska Anchorage, Anchorage, AK 99508-4664, USA*

<sup>13</sup>*Department of Astronomy and Joint Space-Science Institute, University of Maryland, College Park, MD 20742, USA*

This paper has been typeset from a  $\text{\TeX}/\text{\LaTeX}$  file prepared by the author.